arXiv:2211.04503v1 [astro-ph.HE] 8 Nov 2022

The Impact of Cosmic Ray Injection on Magnetic Flux Tubes in a Galactic Disk

Roark Habegger [ID],[1, 2] Ellen G. Zweibel [ID],[1, 2] and Sherry Wong [ID][1, 3]

[1]*University of Wisconsin-Madison Astronomy Department*
[2]*University of Wisconsin-Madison Physics Department*
[3]*University of Wisconsin-Madison Computer Sciences Department*

ABSTRACT

In galactic disks, the Parker instability results when non-thermal pressure support exceeds a certain threshold. The non-thermal pressures considered in the Parker instability are cosmic ray pressure and magnetic pressure. This instability takes a long time to saturate ($> 500\,\mathrm{Myr}$) and assumes a background with fixed cosmic ray pressure to gas pressure ratio. In reality, galactic cosmic rays are injected into localized regions ($< 100\,\mathrm{pc}$) by events like supernovae, increasing the cosmic ray pressure to gas pressure ratio. In this work, we examine the effect of such cosmic ray injection on large scales ($\sim 1\,\mathrm{kpc}$) in cosmic ray magnetohydrodynamic simulations using the `Athena++` code. We vary the background properties, dominant cosmic ray transport mechanism, and injection characteristics between our simulation runs. We find the injection will disrupt the interstellar medium on shorter timescales than the Parker instability. If cosmic ray transport by advection is dominant, cosmic ray injection disrupts the disk on short time scales ($< 100\,\mathrm{Myr}$). If cosmic ray transport by the streaming instability is dominant, the injection creates a buoyant flux tube long after the initial injection ($> 150\,\mathrm{Myr}$). Finally, when cosmic ray transport by diffusion dominates, the injected cosmic rays make an entire flux tube over pressured in a short time ($\sim 10\,\mathrm{Myr}$). This over pressure pushes gas off the tube and drives buoyant rise on time scales similar to the advection dominated case.

Keywords: Galaxy Structure (622) - Cosmic Rays (329) - Magnetohydrodynamical simulations (1966)

1. MOTIVATION

In 1966, Eugene Parker showed the interstellar medium's (ISM's) stratification was unstable when non-thermal pressures were introduced (Parker 1966). Parker considered two non-thermal components: the galactic magnetic field and cosmic rays. This decision was motivated by measurements of the Milky Way's thermal energy density, magnetic energy density, and cosmic ray energy density. Measurements suggest these are all on the order of $\sim 10^{-12}\,\mathrm{erg\,cm^{-3}}$ (Parker 1966; Ruzmaikin et al. 1988; Boulares & Cox 1990; Ferrière 2001; Draine 2011). With the non-thermal pressures (cosmic rays and the magnetic field) and under certain equations of state (EoS), Parker showed the magnetic field would be dragged upward by buoyant parcels of the

Corresponding author: Roark Habegger
rhabegger@wisc.edu

ISM. This buoyant rise creates a feedback loop because the curved magnetic field lines (originally parallel to the disk) provide a slope for gas to slide down into the galactic disk. This process removes more mass from the parcel, increasing the buoyancy force on it. The buoyancy force drives further rising, and the process continues. The end result is the production of magnetic lobes perpendicular to the galactic disk and pockets of dense gas in the disk (Parker 1966). The instability's movement of gas upward could also create mass loss from the disk. If cosmic ray pressure is driving the instability, then this effect is an example of cosmic ray driven winds, a process included in some global galactic evolution simulations (Everett et al. 2008; Uhlig et al. 2012; Ruszkowski et al. 2017; Farber et al. 2018; Zhang 2018; Hopkins et al. 2018; Chan et al. 2019). Additionally, cosmic rays can be a significant component of stellar feedback by heating and disrupting gas clouds (Farber et al. 2018; Bustard & Zweibel 2021; Kempski & Quataert 2021). The Parker instability also influences the galactic dynamo because

it changes the structure of the galactic magnetic field: it bends field lines, growing the component of the field perpendicular to the disk (Hanasz & Lesch 2000, 2003; Hanasz et al. 2013).

While the non-thermal pressure in cosmic rays and aforementioned buoyancy mechanism provide a way for cosmic rays to affect galactic evolution, there is evidence against the Parker instability being a dominant force in galaxies. The original Parker instability setup has been revisited, often including more physical processes and more realistic setups (Mouschovias 1974; Zweibel & Kulsrud 1975; Asseo et al. 1978; Giz & Shu 1993; Heintz & Zweibel 2018; Heintz et al. 2020). Overall, these additional considerations show the Parker instability has a longer growth time than originally estimated, and it takes up to 500 Myr to saturate. These results also place more stringent criteria for a galaxy to be Parker unstable, meaning more galactic disks are likely to not experience the instability. When a galaxy's ISM is Parker unstable, the long saturation time means any structure created by the instability could become overshadowed by other mechanisms with shorter timescales like galactic rotation, spiral density waves, and supernovae. The key difference between the different analyses is the gas EoS and the cosmic ray EoS. Making either EoS stiffer (higher adiabatic index γ_g (gas) or γ_c (cosmic rays)) will make the system more stable. A softer EoS will destabilize the system. Parker's original assumption a cosmic ray fluid with $\gamma_c = 0$ makes the system very unstable (Heintz & Zweibel 2018). There is an additional consideration in determining the cosmic ray adiabatic index γ_c: it depends on how the cosmic rays are transported (Wiener et al. 2017). As a result of this dependence, cosmic ray transport determines whether the cosmic rays stabilize or destabilize the system (Zweibel 2017; Heintz & Zweibel 2018).

The fundamental question underlying Parker instability research and cosmic ray driven stellar feedback research is "do cosmic rays change the dynamical evolution of a galaxy?" Previous research gives complicated and even conflicting answers to this question. The primary conflict occurs when comparing results from studies with different cosmic ray transport mechanisms. There are three transport mechanisms: (1) advection with the thermal gas, (2) streaming along the magnetic field, and (3) diffusion through the thermal gas, along the magnetic field. Advection is the simplest - the cosmic rays are stuck to the ISM and move with it, forcing movement in regions with a cosmic ray pressure gradient and interacting according to an adiabatic index $\gamma_c = 4/3$. Streaming and diffusion allow the cosmic rays to move separately from the gas. Streaming transports cosmic

rays along the magnetic field at the local Alfven speed, while also heating the gas, resulting in a soft effective adiabatic index $\gamma_{c,\text{eff}} = 2/3$. Diffusion allows the cosmic rays to move through the gas without heating it, while still forcing the gas through the cosmic ray pressure gradient. In reality, all of these processes should occur in a galaxy. Global simulations of star formation feedback suggest that the observed γ-ray luminosities of galaxies are best fit by diffusive transport with a diffusion coefficient several times larger than the Milky Way value, but the uniqueness of the fit is unclear (Chan et al. 2019). Regardless of which transport mechanism dominates, the saturation time for the Parker instability is still long (~ 500 Myr) in an ISM or galactic evolution context.

Instead of studying the Parker instability directly, we focus on the effect of cosmic rays. Specifically, we examine how cosmic rays made in localized injections of energy (e.g., the shock waves created by a supernova explosion) disrupt the ISM. Localized cosmic ray injection has been studied previously as a driver for the galactic dynamo (Hanasz & Lesch 2000, 2003). It produces structure similar to the Parker instability, with an extended magnetic lobe and gas condensed in parts of the disk. Focusing on the sources of cosmic rays instead of the background led us to ask "*are local cosmic ray injections able to change the ISM on time scales shorter than the Parker instability?*" Additionally, we ask four sub-questions concerning the injection's impact on the ISM:

- (Q1) How does the background medium's stability change the injection's impact?

- (Q2) How does the choice of cosmic ray transport model change the injection's impact?

- (Q3) How do the injection's strength and vertical location change its impact?

- (Q4) How does cosmic ray injection differ from heat injection by a thermal explosion?

By answering these questions, our simulations provide a detailed look at how cosmic rays change the ISM on large scales ($\sim$ kpc) in times shorter than the Parker instability, which can take over 500 Myr to saturate (Heintz et al. 2020). Our detailed study provides the most complete picture of the effect of localized cosmic ray injection on galactic disks by exploring an extended parameter space.

Overall, we show for a stiff cosmic ray EoS, when advection is the dominant cosmic ray transport mechanism, cosmic ray injection can change the ISM and

launch gas on timescales $\lesssim 100\,\text{Myr}$. Cosmic ray transport dominated by streaming (a softer EoS) results in buoyant rising, producing structure similar to the Parker instability on timescales $\gtrsim 150\,\text{Myr}$. Finally, we find that cosmic ray diffusion launches gas buoyantly, changing structure on the same timescales as the advection case. **Essentially, cosmic ray injection will cause significant dynamical change on a short timescale, and the change is larger if diffusion is the dominant cosmic ray transport process.**

The paper is split into six sections including this motivation section. In Section 2, we provide background on the Parker instability and cosmic ray transport. In Section 3 we cover our numerical methods, our initial conditions for cosmic ray magnetohydrodynamic simulations in `Athena++`, and our parameter choices for each simulation run. In Section 4 we present the results of each simulation run. In Section 5 we compare the runs and discuss the implications of our simulations, while answering our four questions concerning various astrophysical parameters. In Section 6 we summarize the paper and provide key takeaways from the work. Readers primarily interested in our results should focus on Figs. 10, 14, 15 and Sections 5 & 6.

In the appendices, we provide further detail for our simulations. In Appendix A, we discuss the boundary conditions of our simulations. In Appendix B, we discuss the dependence of our simulation results on various numerical parameters and our parameter choices for the primary simulations.

2. BACKGROUND

The Parker instability disrupts a magnetohydrostatic equilibrium in the galactic disk Parker (1966). Parker's initial work assumed unrealistic conditions for the Milky Way, given our modern knowledge of the ISM. Many of these assumptions were the focus of future research. Some examples are: Zweibel & Kulsrud (1975) showed a stiff EoS for dynamical pressure was stabilizing, Asseo et al. (1978) focused on the impact of the magnetic field line curvature on the instability's evolution, Giz & Shu (1993) reconsidered the assumption of constant gravitational acceleration above and below the midplane, and Heintz & Zweibel (2018) reconsidered the treatment of cosmic ray transport.

One key assumption Parker made was that the non-thermal pressures (magnetic and cosmic ray) were directly proportional to the gas pressure. He defined constants α and β[‡] such that

$$P_B = \frac{B^2}{2\mu_0} = \alpha P_g \qquad P_c = \beta P_g \qquad (1)$$

This assumption of proportionality ignores the multiphase nature of the ISM as well as the discreteness of cosmic sources, which are thought to be primarily young supernova remnants. For young supernova remnants, $10-20\%$ of the kinetic energy will end up in cosmic rays, accelerated at by the expanding shock front (Caprioli & Spitkovsky 2014). In the region around the supernova, we would then have $\beta \sim 10^2$ instead of $\beta \sim 1$ for the cosmic ray background. However, the assumption of constant ratio is useful for the initial conditions of our simulations.

We use the equilibrium setup from Giz & Shu (1993) as our initial ISM background. This equilibrium ISM setup is illustrated in Fig. 1. We use a smooth gravitational profile

$$g(z) = -g_* \tanh\left(\frac{z}{H_*}\right). \qquad (2)$$

instead of the discontinuous $-g_*\text{Sign}(z)$ profile Parker (1966) used originally. The smooth function in Eqn. 2 poses fewer numerical difficulties than a discontinuous profile (Heintz et al. 2020). In Eqn. 2, the asymptotic vertical gravitational acceleration $g_* > 0$ and the gravitational scale height H_* depend on the structure of the galactic disk's stellar population. In addition to being more realistic, Eqn. 2 is also easier to implement in a computational simulation. The gravitational acceleration is shown as red arrows in Fig. 1.

Assuming a plane-parallel hydrostatic equilibrium, the background gas pressure P_g and gas density ρ are determined by

$$\frac{\partial P_{\text{tot}}}{\partial z} = (1 + \alpha + \beta)\frac{\partial P_g}{\partial z} = \rho(z)g(z) \qquad (3)$$

where P_{tot} is the total pressure; the sum of gas, magnetic, and cosmic ray pressure. We solve for the equilibrium under the influence of the gravitational profile Eqn. 2, using an isothermal equation of state $P_g = c_s^2\rho$ with constant sound speed, and midplane values $P_g(z = 0) = P_{g,0}$, $\rho(z = 0) = \rho_0$. The solution to Eqn. 3 is

$$\frac{P_g(z)}{P_{g,0}} = \frac{\rho(z)}{\rho_0} = f(z) = \text{sech}^\eta\left[\frac{z}{\eta H}\right]. \qquad (4)$$

The solution depends on how the scale height of the gas H relates to the gravitational scale height. The scale

---

[‡] Note Parker's β is **not** the plasma beta. Instead, the parameter α is the inverse of the plasma beta $\beta_{\text{pl}} = P_g P_B^{-1} = \alpha^{-1}$.

height of the gas is

$$H = \frac{c_s^2}{g_*}(1 + \alpha + \beta).$$
(5)

The ratio of the two scale heights $\eta = H_*/H$ is a constant. Taking a limit of Eqn. 4 as $\eta \to 0$ (or equivalently, $H_* \to 0$) recovers the solutions in Parker (1966).

We have assumed the pressures, including magnetic pressure, are homogeneous in surfaces parallel to the xy plane, which is shown as a green plane in Fig. 1. For our simulations, we orient the initial magnetic field in the $\hat{x}$ direction. The magnetic field is shown as a blue arrow in Fig. 1. Using Eqns. 1 & 4 the magnetic field is

$$\vec{B}(z) = \hat{x}\sqrt{2\mu_0 \alpha P_{g,0} f(z)}$$
(6)

Similarly, the cosmic ray pressure is

$$P_c(z) = \beta P_{g,0} f(z).$$
(7)

In Fig. 1, the coordinates $(\hat{x}, \hat{y}, \hat{z})$ map to a galactic disk's cylindrical coordinates. The $\hat{x}$ direction is parallel or anti-parallel to the azimuthal direction $\hat{\phi}$ (depending on whether the magnetic field is oriented clockwise or counter-clockwise around the galactic center), the $\hat{y}$ direction is parallel to the radial direction $\hat{r}$, and the $\hat{z}$ direction is parallel to the cylindrical $\hat{z}$ direction.
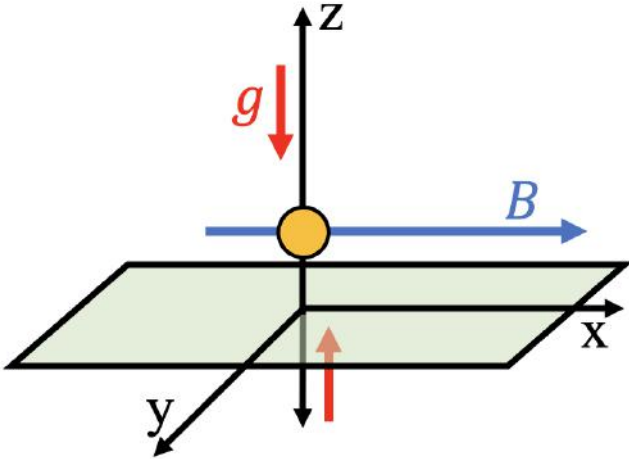
2.1. Parker Instability

Figure 1. This schematic shows our initial setup for hydrostatic equilibrium. We have a gravitational field (red arrows) in the $\hat{z}$ direction, which flips sign at the midplane $z = 0$ (see Eqn. 2). The magnetic field is oriented along the $\hat{x}$ direction and creates a magnetic pressure supporting vertical hydrostatic equilibrium (Eqns. 3,6). We then inject cosmic rays, shown by a yellow circle, above the midplane, shown as a green rectangle (see Sec. 3.2 for injection profile).
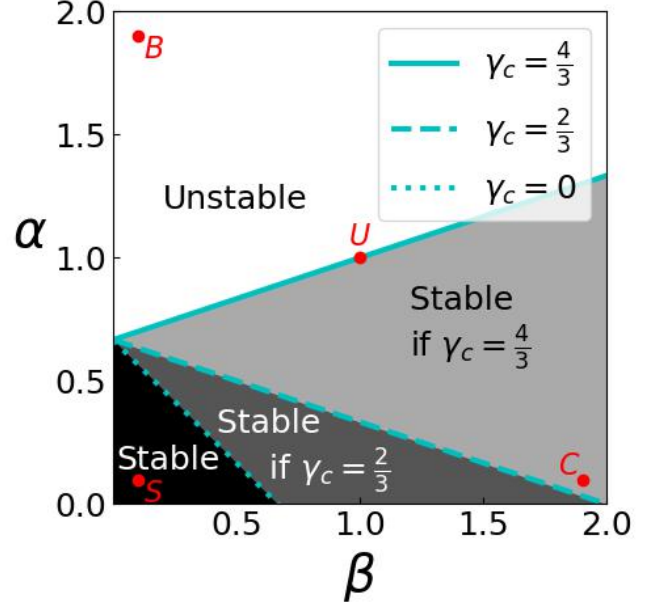

Figure 2. This schematic shows the parameter space of magnetic pressure $\alpha = P_B/P_g$ and cosmic ray pressure $\beta = P_c/P_g$. For three simple transport mechanisms, we show the regions of parameter space where the initial hydrostatic equilibrium (see 2.1) is unstable to the Parker instability. The first transport is the advection of a relativistic gas with $\gamma_c = 4/3$, the second transport mechanism is cosmic ray streaming with an effective $\gamma_c = 2/3$, and the third treats cosmic rays as an infinitely compressible fluid $\gamma_c = 0$. The S, U, B, and C points are where are simulations, in Table 1, are located in this parameter space.

Depending on the values of the parameters α and β, the equilibrium solution may be unstable to small perturbations. We can assess the stability of the medium with the Schwarzschild convection criterion (Newcomb 1961; Boulares & Cox 1990; Zweibel 2017). This criterion for instability in a vertically stratified atmosphere is

$$-\frac{d\ln\rho}{dz} < \frac{\rho g_*}{\gamma_g P_g}.$$
(8)

This criterion is applicable above the midplane with $z > 0$. Assuming we are more than two scale heights above the midplane $z > 2H_*$, then the logarithmic derivative is the scale height H of the gas. Using this assumption and assuming g_* is constant in the same region, the criterion for instability to occur is

$$\alpha + \beta > \gamma_g - 1.$$
(9)

If we include the compressibility of cosmic rays, then we need to replace $\gamma_g P_g \to \gamma_g P_g + \gamma_c P_c$ in Eqn. 8. Using this change and evaluating the criterion again, we get

$$\alpha + \beta(1 - \gamma_c) > \gamma_g - 1.$$
(10)

The above criterion illustrates a confusing result noted in Zweibel (2017), and again in Heintz & Zweibel (2018). Generically, one would guess increasing non-thermal pressures makes the system more unstable. However, Eqn. 10 shows there is a way for increasing cosmic ray pressure (β) to make the system more stable. Since the cosmic ray fluid is relativistic gas, it has $\gamma_c = \frac{4}{3}$ when advection is the dominant transport mechanism. In that case, the left hand side would be smaller with increasing β. However, if cosmic rays are transported via the streaming instability, then the cosmic ray fluid has an effective value $\gamma_{c,\text{eff}} = \gamma_c/2 = \frac{2}{3}$ (Wiener et al. 2017). This transport case leads to a more intuitive result: increasing β makes the system more unstable.

These considerations of stability are summarized in Fig. 2, which is a schematic and not completely predictive of our simulation setup, which has a variable g_* and logarithmic density derivative. The schematic shows the α-β space of equilibrium solutions with an adiabatic gas exponent $\gamma_g = 5/3$. Using Eqns. 9 and 10, we show different regions of stability determined by the effective cosmic ray adiabatic index $\gamma_{c,\text{eff}}$. There is a strictly Parker unstable region (unshaded), a strictly Parker stable region (black), and in the gray regions, stability depends on cosmic ray transport. For smaller values of γ_g, the fan of stability boundaries shifts downward so the boundaries intersect on the vertical axis where $\alpha = \gamma_g - 1$.

2.2. Cosmic Ray Transport

The stability of the system described in Sec. 2.1 and illustrated in Fig. 2 depends on the effective compressibility of the cosmic rays, and therefore on cosmic ray transport. Cosmic rays are transported throughout the interstellar medium by three mechanisms: advection, streaming, and diffusion. Advection is the simplest: if the thermal gas has a bulk flow in a particular direction, the cosmic rays should flow with the gas. If advection is dominant, then the cosmic rays are a relativistic fluid, with negligible mass, following the flow of the thermal (non-relativistic) gas.

Streaming is the result of a gyroresonant instability, wherein cosmic rays generate hydromagnetic waves and scatter off those same waves. This instability appears in kinetic theory for cosmic ray transport, and it drives the cosmic rays into a bulk flow at the Alfven speed $\mathbf{v}_A$. When the gyro-orbit of the cosmic rays is similar in size to the wavelength of an Alfven wave, the cosmic ray will scatter off the wave. This process produces a shift in the cosmic ray distribution function. That shift produces a bulk flow along magnetic field lines, down the (spatial) cosmic ray pressure gradient, at the Alfven speed (Kulsrud & Pearce 1969; Wentzel 1969; Skilling 1975).

In fluid simulations, the streaming instability is often included by adding a velocity

$$\mathbf{v}_s = -\frac{\mathbf{B}}{\sqrt{\mu_0 \rho}} \frac{\mathbf{B} \cdot \boldsymbol{\nabla} P_c}{|\mathbf{B} \cdot \boldsymbol{\nabla} P_c|} = -\mathbf{v}_A \frac{\mathbf{B} \cdot \boldsymbol{\nabla} P_c}{|\mathbf{B} \cdot \boldsymbol{\nabla} P_c|} \quad (11)$$

to the cosmic ray fluid flow (Breitschwerdt et al. 1991; Sharma et al. 2010; Jiang & Oh 2018). The streaming instability heats the gas: the cosmic rays transfer energy to hydromagnetic waves through gyro-resonance, which then dissipate energy into the thermal gas (Kulsrud & Pearce 1969; Wentzel 1969; Skilling 1975). This heating appears as a source term in the equation for the thermal energy density and the cosmic ray energy density. The work done by the cosmic rays on the thermal gas, through the hydromagnetic waves, is a result of the streaming instability is $\mathbf{v}_A \cdot \boldsymbol{\nabla} P_c$ (Breitschwerdt et al. 1991; Jiang & Oh 2018). This work term is in addition to the individual adiabatic compressibility of the thermal fluid and the cosmic rays.

Diffusion of cosmic rays allows the cosmic rays to leak through the thermal gas. Cosmic rays in the Milky Way diffuse through a kiloparsec of gas on the time scale of $\sim 10\,\text{Myr}$. This timescale leads to a diffusion coefficient of $\kappa_c \sim 3 \cdot 10^{28}\,\text{cm}^2\,\text{s}^{-1}$. However, galaxy simulations have suggested higher diffusion coefficients, $\kappa_c > 10^{29}\,\text{cm}^2\,\text{s}^{-1}$, are necessary to match γ-ray observations of other galaxies (Chan et al. 2019).

Each of these transport methods drives a different characteristic response in the ISM when cosmic rays are injected. With a cosmic ray injection, advection and streaming will both drive a steep front of material. However, whereas advection will result in the cosmic ray fluid moving at the flow speed, streaming allows the cosmic rays to move at the Alfven speed, possibly ahead of the gas. Then, the front of cosmic rays can move through the gas it has compressed. Diffusion, in contrast to both streaming and advection, drives a smoother flow of cosmic rays as the injection slowly spreads out through the ISM. Since we vary the magnetic field strength, diffusion coefficient, and thermal adiabatic index γ in our simulations, we provide the following useful timescales for transport through a distance L of the ISM:

$$\tau_{\text{adv}} = L \cdot \left(\frac{\gamma_g P_0}{\rho_0} \right)^{-1/2} \quad (12)$$

$$\tau_{\text{str}} = L \cdot \left(\frac{B_0}{\sqrt{\mu_0 \rho_0}} \right)^{-1} \quad (13)$$

$$\tau_{\text{diff}} = \frac{L^2}{\kappa_c} \quad (14)$$

In our simulations, the gas flows are generally subsonic, so the advection timescale is an imperfect measure: the correct timescale will be larger. For advection dominated simulations, we set the simulation parameters such that the streaming and diffusion timescales are much larger than an order unity multiple of the advection timescale in Eqn. 12. However, when the advection and streaming timescales are similar according to Eqns. 12 & 13, the streaming transport dominates the dynamics in our simulations because of this overestimated flow speed. We only use these timescales to determine the dominant transport mechanism, defaulting to streaming when the streaming and advection timescales are similar (i.e. Simulation U - see Table 1). When calculating these timescales in Table 1, we use a distance $L = 1\,\mathrm{kpc}$ because that is the distance between the injection location and the edge of the simulation in the $\hat{x}$ direction. Therefore, it is the distance the injected cosmic rays need to travel along the magnetic field before leaving the simulations.

3. SETUP: EXPLOSIONS IN A STRATIFIED MEDIUM

To explore how cosmic ray injection affects the ISM, we run simulations using the `Athena++` code (Stone et al. 2020). `Athena++` is a fully parallel general relativistic magnetohydrodynamic code used for simulations of galaxies, stars, accretion disks, jets, ISM clouds, and other astrophysical objects. We use the implementation from Jiang & Oh (2018) which evolves a relativistic fluid (of cosmic rays) with negligible mass alongside the thermal gas. Below, we outline the numerical methods and our initial conditions.

The conservative fluid equations, including a cosmic ray component, are (Stone et al. 2020; Breitschwerdt et al. 1991):

$$\frac{\partial \rho}{\partial t} + \boldsymbol{\nabla} \cdot (\rho \mathbf{v}) = 0 \qquad (15)$$

$$\frac{\partial \mathbf{B}}{\partial t} - \boldsymbol{\nabla} \times (\mathbf{v} \times \mathbf{B}) = 0 \qquad (16)$$

$$\frac{\partial (\rho \mathbf{v})}{\partial t} + \boldsymbol{\nabla} \cdot \left(\rho \mathbf{v}\mathbf{v} + \left(P_g + \frac{1}{2} B^2 \right) \mathbb{1} - \mathbf{B}\mathbf{B} \right)$$
$$= \rho \mathbf{g} - (\gamma_c - 1) \boldsymbol{\nabla} E_c \quad (17)$$

$$\frac{\partial E}{\partial t} + \boldsymbol{\nabla} \cdot \left(\mathbf{v} \left(E + P_g + \frac{1}{2} B^2 \right) - \mathbf{B} \left(\mathbf{B} \cdot \mathbf{v} \right) \right)$$
$$= \rho \mathbf{g} \cdot \mathbf{v} - \frac{\partial E_c}{\partial t} - \boldsymbol{\nabla} \cdot \mathbf{F}_c \quad (18)$$

$$\frac{\partial E_c}{\partial t} + \boldsymbol{\nabla} \cdot \mathbf{F}_c = (\gamma_c - 1) \left(\mathbf{v} + \mathbf{v}_s \right) \cdot \boldsymbol{\nabla} E_c \qquad (19)$$

$$\mathbf{F}_c = \gamma_c \left(\mathbf{v} + \mathbf{v}_s \right) E_c - \hat{\boldsymbol{\kappa}}_c \cdot \boldsymbol{\nabla} E_c \qquad (20)$$

The dynamical variables are density ρ, bulk flow velocity $\mathbf{v}$, gas pressure P_g, magnetic field $\mathbf{B}$, the combined internal and kinetic energy density $E = P/(\gamma_g - 1) + \rho v^2/2$, and the cosmic ray energy density $E_c = P_c/(\gamma_c - 1)$. There is a fixed expression (Eqn. 20) for the cosmic ray flux $\mathbf{F}_c$, which contains the rank-2 diffusion tensor $\hat{\boldsymbol{\kappa}}_c$. The rank-2 identity tensor (or Kronecker delta) is $\mathbb{1}$. Bold variables are all vectors (rank-1 tensors), with three components. The gravitational acceleration $\mathbf{g} \propto \hat{z}$ is given by Eqn. 2. Others mix the use of P_c and E_c (see the Appendix of Breitschwerdt et al. (1991) for canonical equations). Here, we have written everything in terms of E_c to emphasize that it is the conservative dynamic variable used in the simulation. Note these equations are in units with $\mu_0 = 1$, unlike the Gaussian-cgs units used in Breitschwerdt et al. (1991).

Solving these equations requires additional numerical work compared to the case with no cosmic rays involved. In particular, the streaming instability requires new methods to avoid numerical problems at maxima in cosmic ray pressure (Sharma et al. 2010). We use the implementation of cosmic rays in `Athena++` presented in Jiang & Oh (2018). In this implementation, the cosmic ray flux is a separate variable. This two moment method inspired by radiative transfer (Jiang et al. 2014) makes the code more accurate and numerically stable near peaks in cosmic ray energy density. Neglecting the continuity (Eqn. 15) and induction (Eqn. 16) equations, which do not change in this implementation, the actual equations we solve in `Athena++` are:

$$\frac{\partial (\rho \mathbf{v})}{\partial t} + \boldsymbol{\nabla} \cdot \left(\rho \mathbf{v}\mathbf{v} + \left(P_g + \frac{1}{2} B^2 \right) \mathbb{1} - \mathbf{B}\mathbf{B} \right)$$
$$= \rho \mathbf{g} + \hat{\boldsymbol{\sigma}}_c \cdot \left(\mathbf{F}_c - \frac{4}{3} \mathbf{v} E_c \right) \quad (21)$$

$$\frac{\partial E}{\partial t} + \boldsymbol{\nabla} \cdot \left(\mathbf{v} \left(E + P_g + \frac{1}{2} B^2 \right) - \mathbf{B} \left(\mathbf{B} \cdot \mathbf{v} \right) \right)$$
$$= \rho \mathbf{g} \cdot \mathbf{v} - \frac{1}{3} \left(\mathbf{v} + \mathbf{v}_s \right) \cdot \boldsymbol{\nabla} E_c \quad (22)$$

$$\frac{\partial E_c}{\partial t} + \boldsymbol{\nabla} \cdot \mathbf{F}_c = \frac{1}{3} \left(\mathbf{v} + \mathbf{v}_s \right) \cdot \boldsymbol{\nabla} E_c \qquad (23)$$

$$\frac{1}{V_m^2} \frac{\partial \mathbf{F}_c}{\partial t} + (\gamma_c - 1) \boldsymbol{\nabla} E_c = -\hat{\boldsymbol{\sigma}}_c \cdot \left(\mathbf{F}_c - \frac{4}{3} \mathbf{v} E_c \right) \qquad (24)$$

This implementation automatically treats the cosmic rays as a relativistic fluid with $\gamma_c = 4/3$. There are two
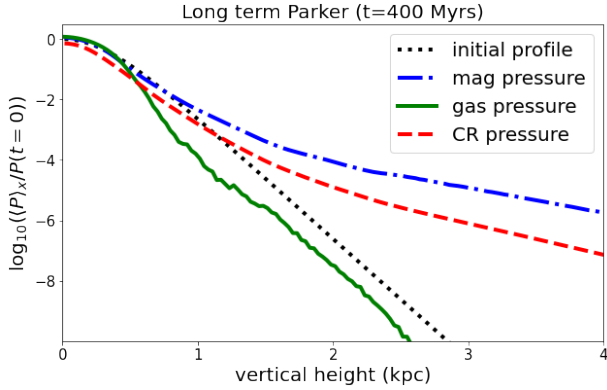
Figure 3. Magnetic (blue, dash-dotted line), gas (green, solid line, and cosmic ray (red, dashed line) pressure averaged over horizontal distance x for $\alpha = 10/3$ & $\beta = 1.25$. All pressures start at the same initial profile shape, shown as a black, dotted line. Gas pressure is compressed towards the midplane whereas cosmic ray and magnetic pressures spread out of the disk.

key changes here. First, the diffusion tensor $\hat{\boldsymbol{\kappa}}_c$ is replaced by $\hat{\boldsymbol{\sigma}}_c$; the components of this tensor have units of time/length^2, so they are determined by the reciprocal of the diffusion rates in each direction. Second, Jiang & Oh (2018) introduced a modified speed of light V_m with the variable cosmic ray flux. Modifying the speed of light allows the simulations to be more efficient by avoiding the stiff time limit imposed by using the actual speed of light. Since this parameter is arbitrary (at a minimum it must be larger than any other velocities in the simulation), we consider the convergence of our simulations for different values of V_m in Appendix B.

3.1. Comparison with Parker Instability Simulations

To test our numerical methods and initial conditions, we ran a 2D simulation matching one in Heintz et al. (2020). Those simulations used the FLASH code (Fryxell et al. 2000), along with the streaming transport method in Sharma et al. (2010). Matching those parameters (originally based on Rodrigues et al. (2016)), we use $\rho_0 = 6.76 \cdot 10^{-25}\,\text{g}\,\text{cm}^{-3}$, $P_{g,0} = 8.19 \cdot 10^{-13}\,\text{erg}\,\text{cm}^{-3}$, $g_* = 2 \cdot 10^{-9}\,\text{cm}\,\text{s}^{-2}$, $\eta = 2$, $H = 250\,\text{pc}$, $\alpha = 10/3$, $\beta = 1.25$, and $V_m = 0.01c$. We find that that our simulation method is consistent with that of Heintz et al. (2020), and our results are illustrated in Fig. 3. Fig. 3 compares horizontally averaged profiles of the various pressure components at a highly nonlinear stage of the instability with their original profiles. The magnetic and cosmic ray pressures decrease more slowly away from the plane as the magnetic field becomes bent, while gas pressure is compressed towards the midplane. Gravity pulls the gas down along the magnetic flux tubes, which have

turned perpendicular to the disk in several locations. Our simulation matches expected behavior (see Fig. 11 of Heintz et al. (2020), a similar plot but at a time of $500\,\text{Myr}$) and evolves on a similar time scale. This result shows that our initial background conditions agree with other Parker simulations. Additionally, it shows the cosmic ray evolution method implemented in `Athena++` by Jiang & Oh (2018) is accurate for this setup and the current investigation, since it is in reasonable agreement with the FLASH code's implementation of cosmic rays (Fryxell et al. 2000; Sharma et al. 2010; Heintz et al. 2020).

3.2. Initial Conditions for Injection Simulations

The initial profiles of density, gas pressure, magnetic field, and cosmic ray pressure are described in Sec. 2. We use midplane density and pressure values of $\rho_0 = 10^{-24}\,\text{g}\,\text{cm}^{-3}$ and $P_{g,0} = 10^{-12}\,\text{g}\,\text{cm}^{-3}$. We use an asymptotic gravitational acceleration $g_* = 4 \cdot 10^{-9}\,\text{cm}\,\text{s}^{-2}$ and a gravitational scale height $H_* = 100\,\text{pc}$. We use a smaller gravitational scale height for the injection simulations (compared to $H_* = 500\,\text{pc}$ in Sec. 3.1) because we want the injection to move under a constant gravitational acceleration. This change, along with increasing the gravitational acceleration, makes it harder for buoyancy to overpower the gravitational force on the gas. Using similar pressures as the Parker simulation in Sec. 3.1, our initial profile's height ratio η (see Eqn. 4) is smaller than expected in the Milky Way. As previously mentioned, $\gamma_c = 4/3$, since the streaming instability is included explicitly in the implementation by Jiang & Oh (2018). Therefore, changing γ_c to $\gamma_{c,\text{eff}} = \gamma_c/2$ would be redundant and over-estimate the impact of streaming.

The simulation grid is $200 \times 50 \times 300$ cells (ordered with respect to $(\hat{x}, \hat{y}, \hat{z})$) . The cell size is $10 \times 20 \times 10\,\text{pc}^3$, giving a total simulation volume $2 \times 1 \times 3\,\text{kpc}^3$. The second dimension is off-center of the midplane ($z = 0$), extending from $z = -1\,\text{kpc}$ to $z = +2\,\text{kpc}$. The cosmic rays are injected above the midplane ($z > 0$), so this off-centering focuses the computational resources on the injection and the resulting flows. We do not use any adaptive or static mesh refinement.

The cosmic ray injection profile is a 3D Gaussian function:

$$\varepsilon_c(x, y, z) = \frac{E_{\text{SN}}}{(2\pi r_{\text{SN}}^2)^{3/2}} \cdot \exp\left[\frac{-1}{2r_{\text{SN}}^2}|\vec{x} - \vec{x}_0|^2\right]. \quad (25)$$

The parameters of the injection are its position $\vec{x}_0$, radius r_{SN}, and total energy injected E_{SN}. The formula is for cosmic ray energy density ε_c. We add this perturbation onto the background cosmic ray pressure profile

in Eqn. 7. Integrating the profile, Eqn. 25, over volume gives E_{SN} as the total energy injected. The injection occurs at different heights above the midplane depending on the other parameters under consideration (see Table 1).

In each simulation, we use the same injection radius $r_{SN} = 50\,pc$. This radius is large for a single supernova shock, but we will end up considering cosmic ray injection from multiple supernova (see Sec. 3.3) in the same volume. This larger radius would then contain ~ 10 supernovae. Additionally, this radius allows our simulation (with $10 - 20\,pc$ resolution) to reliably sample the injection profile. To avoid sampling errors (aliasing) which will change the total injected energy, we center the injection in the xy plane on a cell. The grid has cell faces along $x = 0$ and $y = 0$ planes, so we choose to center the injection at $x_0 = 5\,pc$ and $y_0 = 10\,pc$. As a result, the peak of the profile occurs in the center of a computational cell. The height z_0 and total energy E_{SN} are varied across our simulations (see Table 1).

3.3. *Justification of Parameters*

We present the results of several simulations of cosmic ray injection in a cosmic ray magnetohydrodynamic version of Athena++ (see Jiang & Oh (2018)). Table 1 shows the list of our simulations with their critical parameters and our labels for them. The simulations help us answer several questions, presented in the introduction and repeated here for convenience:

- (Q1) How does the background medium's stability change the injection's impact?

- (Q2) How does the choice of cosmic ray transport model change the injection's impact?

- (Q3) How do the injection's strength and vertical location change its impact?

- (Q4) How does cosmic ray injection differ from heat injection by a thermal explosion?

We chose parameters such that our simulations would answer these questions. We first considered what values of α and β are reasonable in the Milky Way galaxy. In our galaxy, measurements suggest the pressures (thermal, cosmic ray, and magnetic) are nearly equal (Ruzmaikin et al. 1988). Therefore, we choose a base run with $\alpha = \beta = 1$. Simulations with these values are named with a prefix U. In Fig. 2, this is on a stability boundary when cosmic ray streaming is not included. However, each simulation in Table 1 includes transport by streaming (even when it is not dominant). Therefore, $\gamma_{c,eff} \leq 4/3$, which suggests this equal pressure

case is Parker unstable. To compare this case with a strictly Parker stable case, we run a simulation with $\alpha = \beta = 0.1$. We use a prefix 'S' to refer to this combination of values. Our first two simulations, labelled U and S, allow us to determine how the stability of the background medium changes the effect of cosmic ray injection. For both these simulations, we use a gas adiabatic constant consistent with a monatomic ideal gas $\gamma_g = 5/3$, a negligible cosmic ray diffusion constant $\kappa_c = 3 \cdot 10^{24}\,cm^2\,s^{-1}$, and an injection energy equivalent to the total kinetic energy ($\sim 10^{51}\,erg$) injected into the ISM by a single supernova. However, only $10\% - 20\%$ of the kinetic energy of a supernova ends up in cosmic rays (Caprioli & Spitkovsky 2014). On the timescale we are considering (millions of years), it is more likely to expect a cloud of star formation to produce multiple supernovae in a localized volume in a time shorter than we resolve. Therefore, our chosen injection energy is $\sim 10\%$ of the energy output by ~ 10 supernovae exploding in the same volume. Our third simulation has the same parameters as U except for the adiabatic gas constant $\gamma_g = 1.1$, which brings the system closer to the isothermal case originally considered by Parker (1966). We name this simulation U-iso. Note that remaking Fig. 2 with this adiabatic constant would shift all the stability boundaries down. Therefore, the equipartition case of $\alpha = \beta = 1$ used in U-iso is strictly Parker unstable.

To answer Q2, we need a way to differentiate the dominant cosmic ray transport mechanism. We estimate the dominant transport mechanism by considering each transport's timescale, given by Eqns. 12, 13, 14. The flows in our simulations are subsonic and our advection timescale assumes propagation at the sound speed. So, when streaming and advection timescales are close, we assume streaming will dominate. Our first two simulations, named U and S, are instances of streaming and advection dominance, respectively. To completely isolate the impact of each transport mechanism, we probe two other points in the $\alpha - \beta$ plane of Fig. 2. We run a simulation with a large magnetic field $\alpha = 1.9$ and low amount of background cosmic rays $\beta = 0.1$, so it is in the top left corner of Fig. 2. This simulation is labelled B-str, and streaming dominates the transport of the injected cosmic rays because the Alfven speed is much higher than the flow speed and the diffusion rate. We also run a simulation C-adv with $\alpha = 0.1$ and $\beta = 1.9$, placing it in the bottom right hand corner of Fig. 2. With this simulation, we probe a Parker stable medium with large non-thermal pressure where streaming is a subdominant transport mechanism. The simulation C-diff has the same values of α and β, but uses a diffusion constant $\kappa = 3 \cdot 10^{28}\,cm^2\,s^{-1}$ which is

| Parameters | | | | | | | | Timescales ($L = 1\,\mathrm{kpc}$) | | |

| $\rho_0 = 10^{-24}\,\mathrm{erg\,cm^{-3}}$ | $H_* = 100\,\mathrm{pc}$ | $V_m = 0.3c$ | $\tau_{\mathrm{adv}} = 76\,\mathrm{Myr}\sqrt{(5/3)/\gamma_g}$ |

$\rho_0 = 10^{-24}\,\mathrm{erg\,cm^{-3}}$ $H_* = 100\,\mathrm{pc}$ $V_m = 0.3c$ $\tau_{\mathrm{adv}} = 76\,\mathrm{Myr}\sqrt{(5/3)/\gamma_g}$

$P_0 = 10^{-12}\,\mathrm{erg\,cm^{-3}}$ $g_* = 4\cdot10^{-9}\,\mathrm{cm\,s^{-2}}$ $\kappa_{c,\perp} = 3\cdot10^{24}\,\frac{\mathrm{cm^2}}{\mathrm{s}}$ $\tau_{\mathrm{str}} = 69\,\mathrm{Myr}\sqrt{1/\alpha}$

$c_s = 10^6\,\mathrm{cm\,s^{-1}}$ $r_{\mathrm{SN}} = 50\,\mathrm{pc}$ $\gamma_c = 4/3$ $\tau_{\mathrm{diff}} = 10\,\mathrm{Myr}\left(10^{28}\frac{\mathrm{cm^2}}{\mathrm{s}}/\kappa_c\right)$

$T = 1.21\cdot10^4\,\mathrm{K}\,(\bar{m}/m_p)$ $B_0 = 5.06\,\mu\mathrm{G}\sqrt{\alpha}$

Run Name	α	β	γ_g	H (pc)	η	z_0 (pc)	Weight ($M_\odot$)	E_{SN} (erg)	CR	$\kappa_{c,\parallel}$ ($\mathrm{cm^2\,s^{-1}}$)	Section
S	0.1	0.1	5/3	97	1.03	45	$1.28\cdot10^4$	10^{51}	Adv.	$3\cdot10^{24}$	Q1
U	1.0	1.0	5/3	243	0.41	105	$2.24\cdot10^4$	10^{51}	Str.	$3\cdot10^{24}$	Q1,Q3,Q4
U-iso	1.0	1.0	1.1	243	0.41	105	$2.24\cdot10^4$	10^{51}	Str.	$3\cdot10^{24}$	Q1
C-adv	0.1	1.9	5/3	243	0.41	105	$2.24\cdot10^4$	10^{51}	Adv.	$3\cdot10^{24}$	Q1,Q2
B-str	1.9	0.1	5/3	243	0.41	105	$2.24\cdot10^4$	10^{51}	Str.	$3\cdot10^{24}$	Q1,Q2
C-diff	0.1	1.9	5/3	243	0.41	105	$2.24\cdot10^4$	10^{51}	Diff.	$3\cdot10^{28}$	Q1,Q2
U-heavy	1.0	1.0	5/3	243	0.41	25	$3.27\cdot10^4$	10^{51}	Str.	$3\cdot10^{24}$	Q3
U-blast	1.0	1.0	5/3	243	0.41	105	$2.24\cdot10^4$	10^{52}	Str.	$3\cdot10^{24}$	Q3
U-therm	1.0	1.0	5/3	243	0.41	105	$2.24\cdot10^4$	$10^{51\,*}$	Str.	$3\cdot10^{24}$	Q4

Table 1. The first table shows the parameters held fixed across our simulations, as well as derived timescales. The second table shows the parameters we vary for each simulation run we perform. The first column shows each simulation run name. The next columns show background medium parameters: magnetic pressure to gas pressure ratio α, cosmic ray pressure to gas pressure ratio β, thermal adiabatic index γ_g, gas scale height H, and profile exponent η (see Eqn. 4). The second set of columns shows injection parameters: initial height of the injection z_0, the weight in the column above the injection, and the volume integrated injection energy E_{SN} (see Eqn. 25), The third set of columns shows dominant cosmic ray transport mechanism, and the parallel cosmic ray diffusion coefficient $\kappa_{c,\parallel}$. The final column shows which questions the simulation applies to (see Sec. 1 & 3.3).

closer to estimated Milky Way values. These three simulations allow us to isolate how streaming, advection, and diffusion each transport the cosmic ray injection. Additionally, B-str and C-adv give us more information to answer Q1 because they are at different points in the $\alpha\beta$-plane. They have different background cosmic ray and magnetic pressures from simulations U or S, allowing us to learn how that aspect of the background medium changes the impact of cosmic ray injection.

For Q3, we adjust parameters related to the injection. Using simulation U as a control case, we compare each of the following simulation to it and only change single parameters. First, we use simulation U-heavy with the cosmic ray injection at a lower height in the disk, meaning it has more weight above it. Second, we use a simulation, U-blast, with the strength of 10% of 100 supernovae to understand how different amounts of energy injection change the results. Other than the weight above the injection and the injection energy, we keep the variables the same as simulation U, which we compare each of these cases against.

For Q4, we run a simulation, U-therm, with the same initial parameters as the Parker unstable simulation U, except the injection is in thermal pressure instead of in cosmic ray pressure.

In the next section (Sec. 4), we cover each simulation, studying how the cosmic ray injection evolved over time,

along with how it changed the medium around it. In the subsections of Sec. 5 we compare the simulations and provide our answers to questions Q1-Q4.

4. RESULTS: INDIVIDUAL SIMULATIONS

In presenting our results, we focus on a flux tube enclosing the initial injection. Since we use the ideal MHD equations, the gas stays on the flux tube. Also, the injected cosmic rays stay on this flux tube because there is effectively no perpendicular diffusion. The injected cosmic rays then force the rest of gas and background cosmic rays on the flux tube to move. For each simulation, we show quantities averaged along the tube. In Figs. 4, 5, 6 we show the average height change of the flux tube as a solid black line, the average gas pressure as a solid purple line, the average magnetic pressure as a dashed purple line, the average cosmic ray pressure as a dash-dotted purple line, and the average mass as a dotted green line. We also show the highest point along the flux tube at any moment in time as a dashed black line. These quantities help us understand how the injection evolves through time and how it causes the flux tube to change.

For some of the simulations, we show 2D cuts (xz-plane) from the 3D simulations in Figs. 7, 8, 9. These cuts show the gas pressure, horizontal ($\hat{x}$) momentum, and vertical ($\hat{z}$) momentum at different times in the sim-

ulation. We show the magnetic field lines used to define the flux tube in the plots of horizontal momentum. Specifically, we show five field lines. The middle field line is the central axis of the flux tube, and the field lines directly above and below mark the edge of the scalar dye (a distance $r_0 = 50\,\mathrm{pc}$ from the central axis of the flux tube). Therefore, the middle three field lines denote the volume we averaged over to produce Figs. 4, 5, 6. Outside the middle three field lines outlining the flux tube, we plot two more field lines which are a distance $2r_0$ from the central axis. Finally, in Fig. 10, we show the cosmic ray pressure distribution at three different time snapshots for the simulations (C-adv, B-str, C-diff) shown in Figs. 7, 8, 9.

4.1. Simulation S

In simulation S, we injected 10^{51} erg of cosmic rays into a Parker stable medium (see Fig. 2 and Table 1). 'Parker stable' refers to linear, small amplitude perturbations, so we did not necessarily expect the run to be stable against our nonlinear, large amplitude perturbation. However, we found the simulation did return to an equilibrium after the cosmic ray injection dissipated. The flux tube evolution in this simulation is shown in the top panel of Fig. 4.

The injection launches the tube upward, but only in the area near the injection (see the peak height in the top panel Fig. 4). During the explosion and rise, the average magnetic pressure, gas pressure, and mass all decrease. After the injection dissipates along the tube, the average values (except for average cosmic ray pressure) along the flux tube reach new stable values. This new stability results in the flux tube's peak falling back down. The flux tube levels out near its initial height, including the peak region which initially rose rapidly. The decrease in average cosmic ray pressure slows as a result of the injection reaching the edge of the simulation by approximately 76 Myr (see Table 1). At this point, the injected cosmic rays leave the simulation out of the ends of the flux tube.

The middle part of the tube eventually falls back down as a reverse flow propagates into the cavity, which has a lower gas pressure. This flow is seen with the increase in gas density and pressure 80 Myr after the injection. This inflow to the cavity increases the gas density there, reversing the buoyancy the parcel initially felt.

4.2. Simulation U

In simulation U, we injected 10^{51} erg of cosmic rays into a Parker unstable medium (see Fig. 2 and Table 1). In this simulation run, the streaming time is shorter
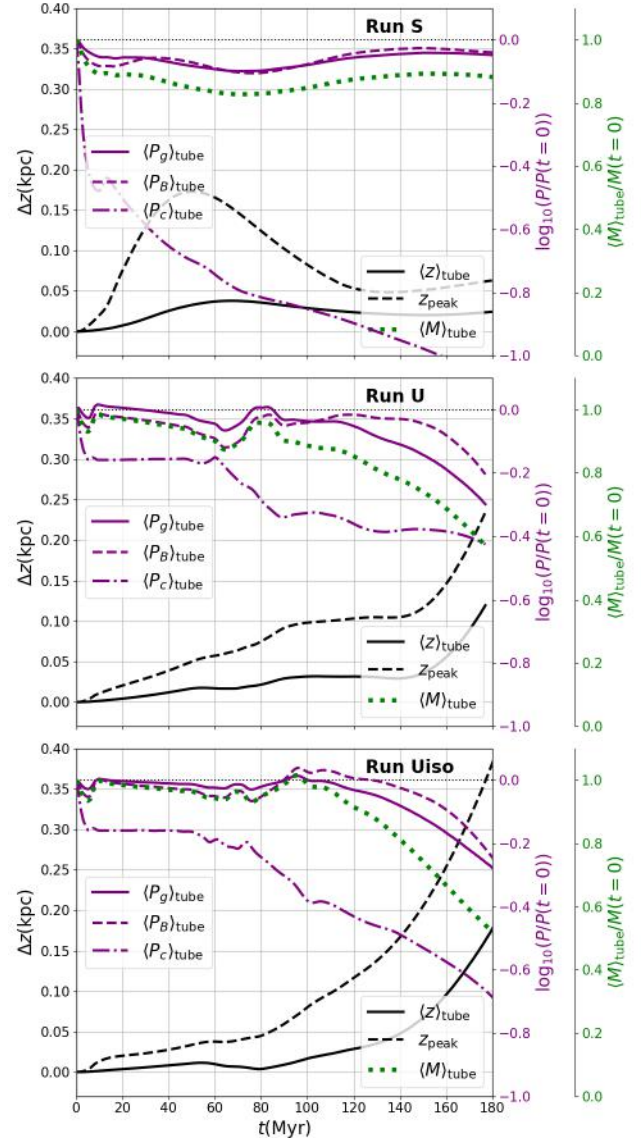

Figure 4. Time evolution of simulations S, U, and U-iso. After injecting cosmic rays on a magnetic flux tube, we track that tube's movement. The solid black line is average height along the length of the tube, whereas the dashed black line is the peak height along the length of the flux tube. The green dotted line is the average mass along the flux tube, as a fraction of the initial average mass along the tube. The purple solid, dashed, and dash-dotted lines are the gas, magnetic, and cosmic ray pressure, respectively, averaged along the length of the flux tube. In simulation S, the flux tube's peak height increases rapidly due to the injection. Eventually though, the peak falls back down and the entire flux tube finds a new equilibrium position. In simulation U, the cosmic ray injection causes the tube to rise only after enough mass has been pushed off the tube. In simulation U-iso, the same process happens except sooner, because it is easier to push the gas off the flux tube.

than the advection time (see Eqns. 12, 13) but they are close in value. The flux tube evolution in this simulation is shown in the middle panel of Fig. 4.

The different time dependence of tube height and average pressures and mass when compared to the top panel of Fig. 4 highlights the change in parameters between simulations S and U. For run U, the streaming cosmic rays heat gas while pushing gas along the flux tube. There is also a reflected wave front which slightly increases the average mass and pressure early in the run. Then, the mass and pressure decrease slowly as the injected cosmic rays move towards the edges of the simulation. Once they reach the boundaries, as early as 60 Myr after the injection, we see the average cosmic ray pressure along the flux tube drop (middle plot of Fig. 4). During this time, the flux tube has slowly been rising near the initial injection location. This increase in peak height is because the cosmic rays took some gas away from the center, leaving it buoyant. This slow buoyant rise creates a new way for gas to move - because the flux tube is bent, the gravitational force pulls gas down the magnetic field lines, toward the disk. This process continues to decrease the average mass along the flux tube. After 140 Myr, the entire flux tube begins to buoyantly rise because it has lost so much mass (see average mass and average flux tube height in middle plot of Fig. 4). Also, the average height and peak height track with each other after approximately 100 Myr. This tracking is characteristic of the entire tube rising buoyantly, not just the central portion where the injection originated.

4.3. *Simulation* U-iso

In simulation U-iso, we injected 10^{51} erg of cosmic rays into a Parker unstable medium (see Fig. 2) with a thermal adiabatic exponent $\gamma_g = 1.1$. In this simulation run, the streaming timescale is shorter than the advection timescale because decreasing γ_g increases the advection timescale (see Eqns. 12, 13). The flux tube evolution in this simulation is shown in the bottom panel of Fig. 4.

While the trends are very similar to simulation U, the bottom panel of Fig. 4 shows buoyant rising even after an increase in average mass above the original value. Additionally, the gas pressure is relatively constant until buoyant rising starts after $\gtrsim 100$ Myr. This constancy of gas pressure is related to the near isothermal nature of the gas. This system should be unstable, and the tube rises despite oscillating up and down early in the simulation. During the start of buoyancy, the magnetic pressure becomes dominant along the tube. This change in dominant pressure also appears in simulation U prior to buoyant rising.

4.4. *Simulation* C-adv

In simulation Cadv, we injected 10^{51} erg of cosmic rays into a Parker stable medium (note $\gamma_c = 4/3$ and see Fig. 2). In this simulation run, the advection timescale is significantly shorter than the streaming time (see Eqns. 12,13) and diffusion is negligible. The lack of streaming dominance transport means the $\gamma_c = 4/3$ boundary in Fig. 2 is more applicable. Therefore, this background medium is Parker stable. The results also mirror the early evolution of simulation S more than simulation U because advection is the dominant transport. The flux tube evolution in this simulation is shown in the top panel of Fig. 5. The rapid rise of the flux tube does not stop in this simulation. The change in background cosmic ray pressure therefore makes the system more prone to disruption by an injection of cosmic rays. In Fig. 7, we show 2D cuts from this 3D simulation.

Immediately after the cosmic ray injection, the tube begins to expand upward (black dashed line in top panel of Fig. 5). This rise is a result of the injection carving a hole in the disk, shown in the first row pressure plot of Fig. 7. Eventually, the average height of the tube also rises dramatically. This rise results from the hole left by the injection pulling the rest of the flux tube up with it (see second row of Fig. 7). This pulling causes more gas to leave the flux tube, further decreasing the mass in the buoyantly rising section. This decrease in average mass after 60 Myr is shown in the top panel of Fig. 7. In Fig. 10, the first column shows how the injection ends up increasing cosmic ray pressure above the disk. This trend is similar to the Parker instability's effect after saturation: spreading the cosmic rays higher above the disk, i.e. giving the cosmic rays a larger scale height.

4.5. *Simulation* B-str

In simulation B-str, we injected 10^{51} erg of cosmic rays into a Parker unstable medium (see Fig. 2). In this simulation run, the streaming timescale is significantly shorter than the advection timescale (see Eqns. 12,13) and diffusion is negligible. The flux tube evolution in this simulation is shown in the middle panel of Fig. 5. In Fig. 8, we show 2D cuts from this 3D simulation.

The streaming heats the gas along the flux tube, which is shown by the increase in average gas pressure early in the simulation, shown in the middle panel of Fig. 5. In the first row gas pressure panel of Fig. 8, the hole created by the injection is shallower than in the C-adv simulation (compare central pressure to the same plot in Fig. 7). Therefore, the hole takes longer to rise. Since the rise is slow, the effect of bending field lines and gravity pulling gas down toward the disk becomes important,
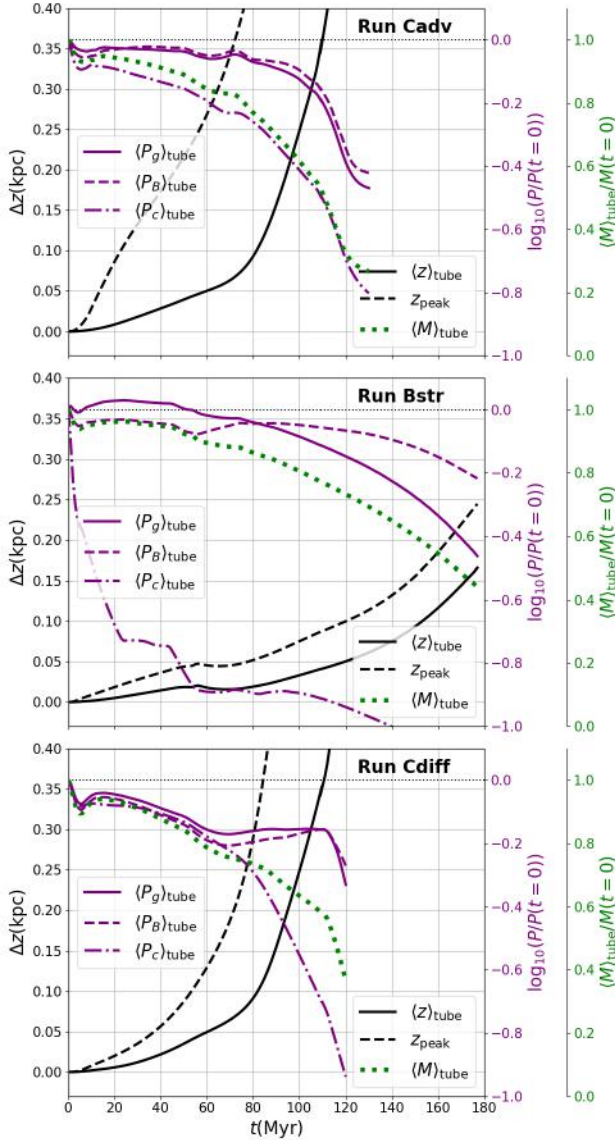
Figure 5. Time evolution of simulations C-adv, B-str, and C-diff. After injecting cosmic rays on a magnetic flux tube, we track that tube's movement. The solid black line is average height along the length of the tube, whereas the dashed black line is the peak height along the length of the flux tube. The green dotted line is the average mass along the flux tube, as a fraction of the initial average mass along the tube. The purple solid, dashed, and dash-dotted lines are the gas, magnetic, and cosmic ray pressure, respectively, averaged along the length of the flux tube. In simulation C-adv, the flux tube's peak height increases rapidly due to the injection. Eventually, the rest of the tube follows this explosive launching. In simulation B-str, the cosmic ray injection heats gas and pushes it down and off the flux tube. Then, the flux tube rises buoyantly. In simulation C-diff, the injection diffuses along the flux tube, driving a large flow of gas off the tube. The central region of the tube then rises buoyantly, eventually pulling the rest of the tube with it.

as in simulations U and U-iso. The flow of gas from this process is shown in the horizontal ($\hat{x}$) momentum plots in the second and third rows of Fig. 8. This flow produces a buoyant rise, as the peak and average height increase together in Fig. 5. The buoyant rise becomes significantly more effective when the magnetic pressure becomes dominant along the tube, a correlation which also appeared in simulations U and U-iso. While the average cosmic ray pressure along the tube decreases, the overall ambient cosmic ray pressure gradient becomes weaker. This trend appears in the middle column of Fig. 10, and matches the expected trend for the Parker instability where the cosmic rays end up with a larger scale height than the gas.

4.6. Simulation C-diff

In simulation C-diff, we injected 10^{51} erg of cosmic rays into a Parker unstable medium (see Fig. 2) with a diffusion constant $\kappa_c = 3 \cdot 10^{28}\,\mathrm{cm}^2\,\mathrm{s}^{-1}$. In this simulation run, the diffusion timescale is much shorter than the advection or streaming timescales (see Eqns. 12,13,14). As a result, the initial Gaussian injection of cosmic rays quickly spreads along the flux tube. This spread drives flow throughout the flux tube, instead of just at its center. The flux tube evolution in this simulation is shown in the bottom panel of Fig. 5. In Fig. 9, we show 2D cuts from this 3D simulation.

Similar to both the advection (C-adv) and streaming cases (B-str) the diffusion creates a hole in the disk, shown in the first row gas pressure plot of Fig. 9. However, this hole is wider than in either of the other cases. As a result, a wider swath of the flux tube begins to buoyantly rise. This buoyant rise is shown by the shape of the peak height in the bottom panel of Fig. 5. This rise of a peak creates a slope for the excess cosmic ray pressure to continue pushing gas off the tube. The main difference between this case and the C-adv case is the gas and magnetic pressure decrease with the cosmic ray pressure throughout. This decrease shows the tube is maintaining pressure equilibrium with its surroundings, while losing mass; this is characteristic of buoyant rising for the central part of the tube. Eventually, the tube has risen significantly and changed the orientation of the magnetic field (see third row horizontal momentum panel of Fig. 9). In the third column of Fig. 10, the cosmic ray pressure has increased about the disk, so this simulation also gives the cosmic ray pressure a larger scale height, similar to a saturated Parker instability.

4.7. Simulation U-heavy

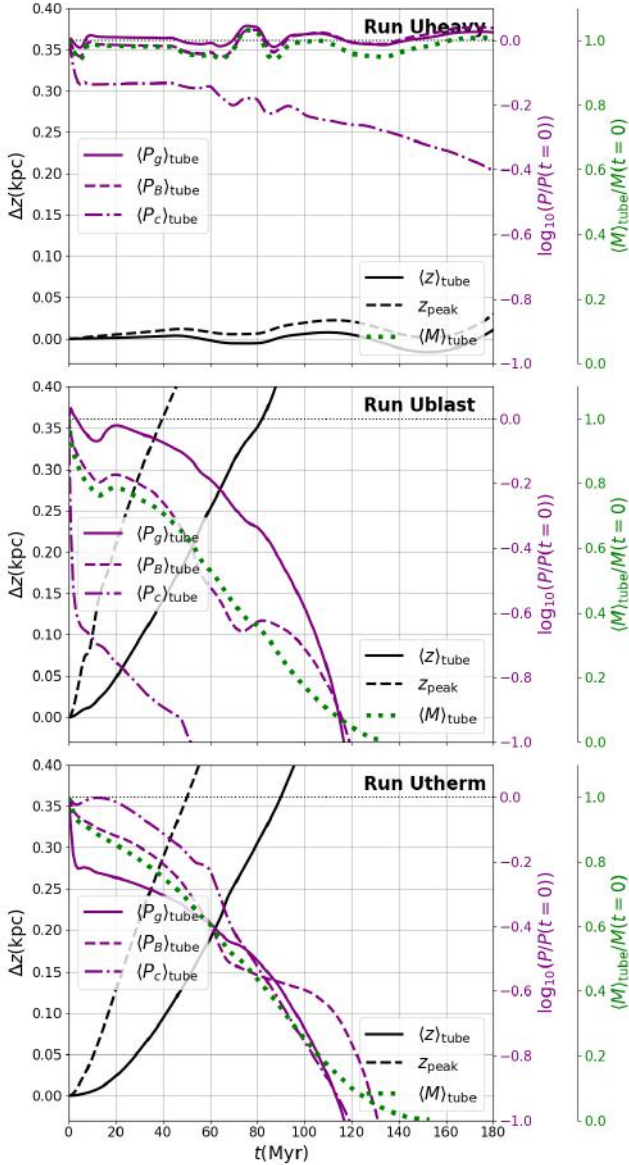In simulation U-heavy, we injected 10^{51} erg of cosmic rays into a Parker unstable medium (see Fig. 2) with

Figure 6. Time evolution of simulations `U-heavy`, `U-blast`, and `U-therm`. After injecting cosmic rays on a magnetic flux tube, we track that tube's movement. The solid black line is average height along the length of the tube, whereas the dashed black line is the peak height along the length of the flux tube. The green dotted line is the average mass along the flux tube, as a fraction of the initial average mass along the tube. The purple solid, dashed, and dash-dotted lines are the gas, magnetic, and cosmic ray pressure, respectively, averaged along the length of the flux tube. In simulation `U-heavy`, the tube fails to rise. In simulation `U-blast`, the cosmic ray injection causes the tube to rise rapidly, because so much cosmic ray energy was injected. In simulation `U-therm`, the tube rises rapidly because the increased gas pressure is more effective than cosmic ray injection at decreasing the magnetic flux tube's mass.

exactly the same parameters as simulation `U`. In this simulation (`U-heavy`), the injection is 25 pc above the disk, instead of 105 pc above the midplane (simulation `U`). The integrated weight above the injection is 1.46 times higher than in simulation `U` (see Table 1). However, the initial gravitational acceleration is less than in simulation `U`. As a result of the increased mass above the tube and the increasing gravitational acceleration felt as the tube rises, the buoyant upward flow takes longer to develop after the injection. The flux tube evolution in this simulation is shown in the top panel of Fig. 6.

In this simulation, the tube oscillates up and down for a long time, compared to the other simulations. However, the increase towards the edge of the top panel of Fig. 6 is the last oscillation. By 220 Myr, the tube's peak height has risen to 0.2 kpc. This takes a longer time than the tube's movement in simulation `U`, which is to be expected because there is more mass above this injection. It also must climb out of a lower point in the gravitational potential.

4.8. *Simulation* `U-blast`

In simulation `U-blast`, we injected 10^{52} erg of cosmic rays into a Parker unstable medium (see Fig. 2), with other parameters matching simulation `U`. This injection is 10 times the energy injected in simulation `U` (see Table 1). As a result, the dynamics in this simulation are more violent. The flux tube evolution in this simulation is shown in the middle panel of Fig. 6.

In the middle panel of Fig. 6, we show the evolution of several tube averaged quantities for simulation `U-blast`. The tube rises fast as the explosion drives a flow upward and moves mass off the center of the tube. However, very quickly, the explosion has blown the tube apart. The central peak of the flux tube reaches the upper boundary of the simulation after ~ 80 Myr, leaving the rest of the flux tube where the injection has not propagated.

4.9. *Simulation* `U-therm`

In simulation `U-therm`, instead of injecting cosmic rays we injected energy as thermal heating. This thermal energy injection had the same magnitude, 10^{51} erg, as the cosmic ray injection in simulation `U`. Just as in simulation `U`, we injected the thermal energy into a Parker unstable medium (see Fig. 2), as in simulation `U`. The thermal injection launches mass faster than the cosmic ray injection. The flux tube evolution in this simulation is shown in the bottom panel of Fig. 6.
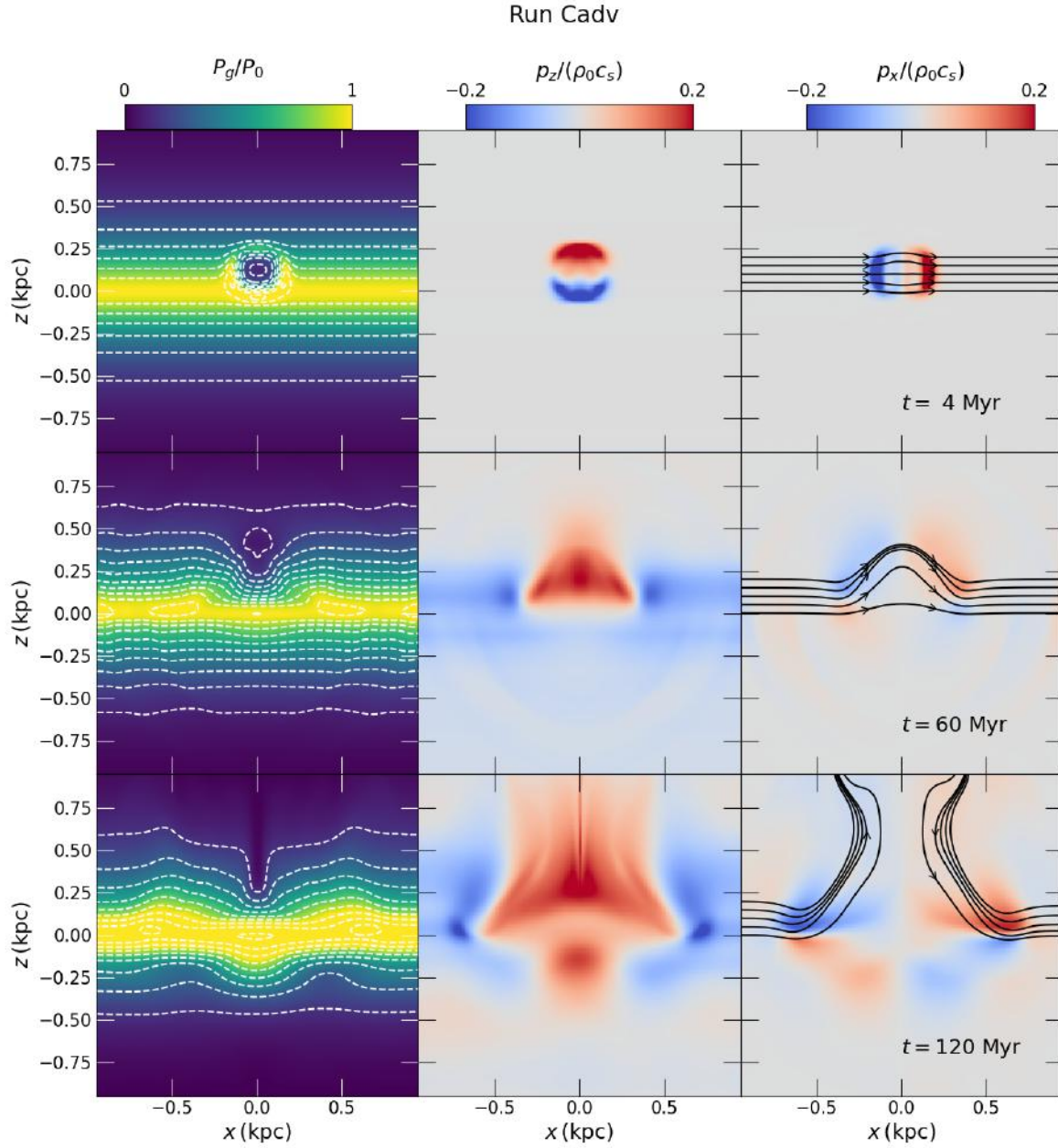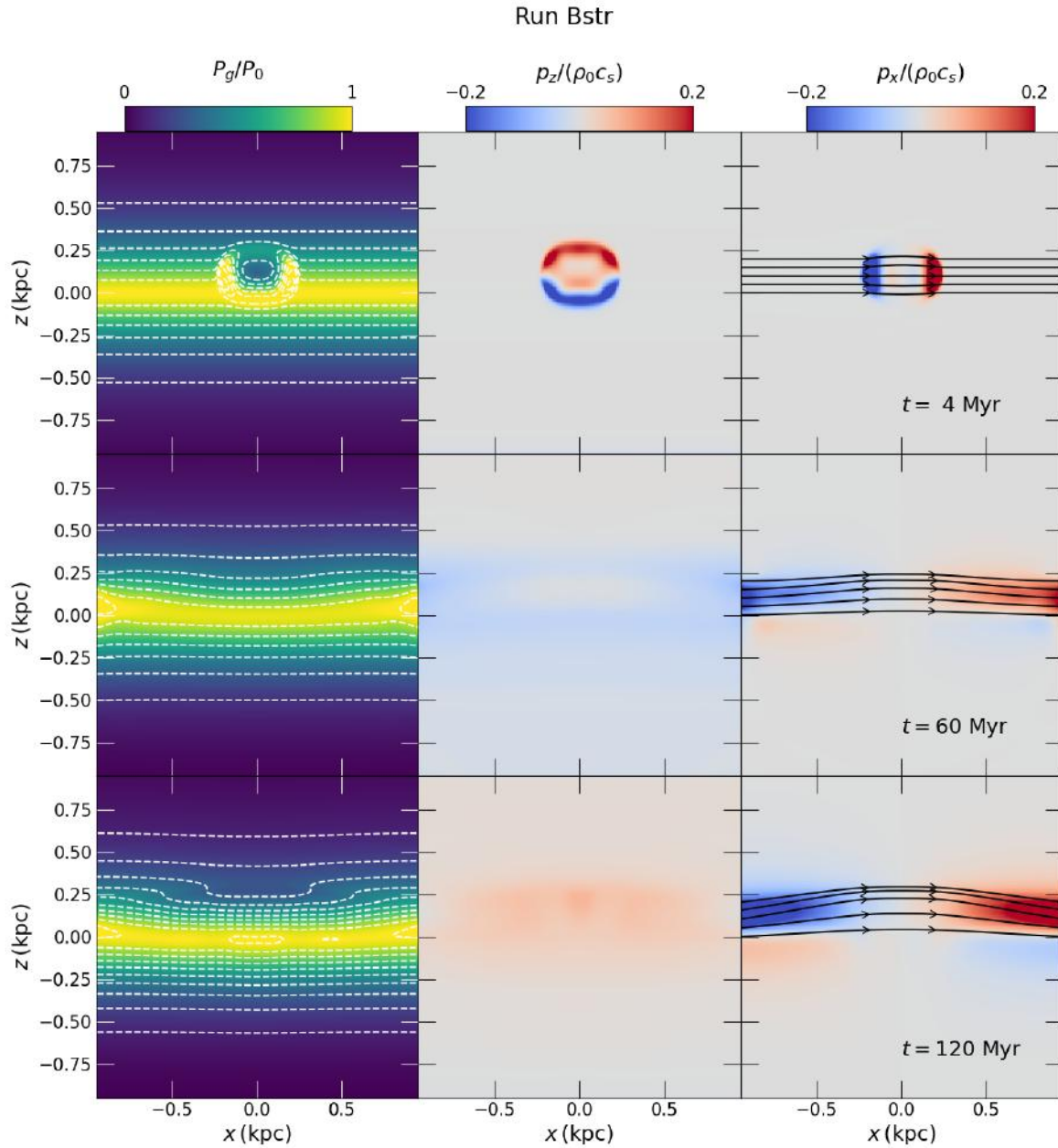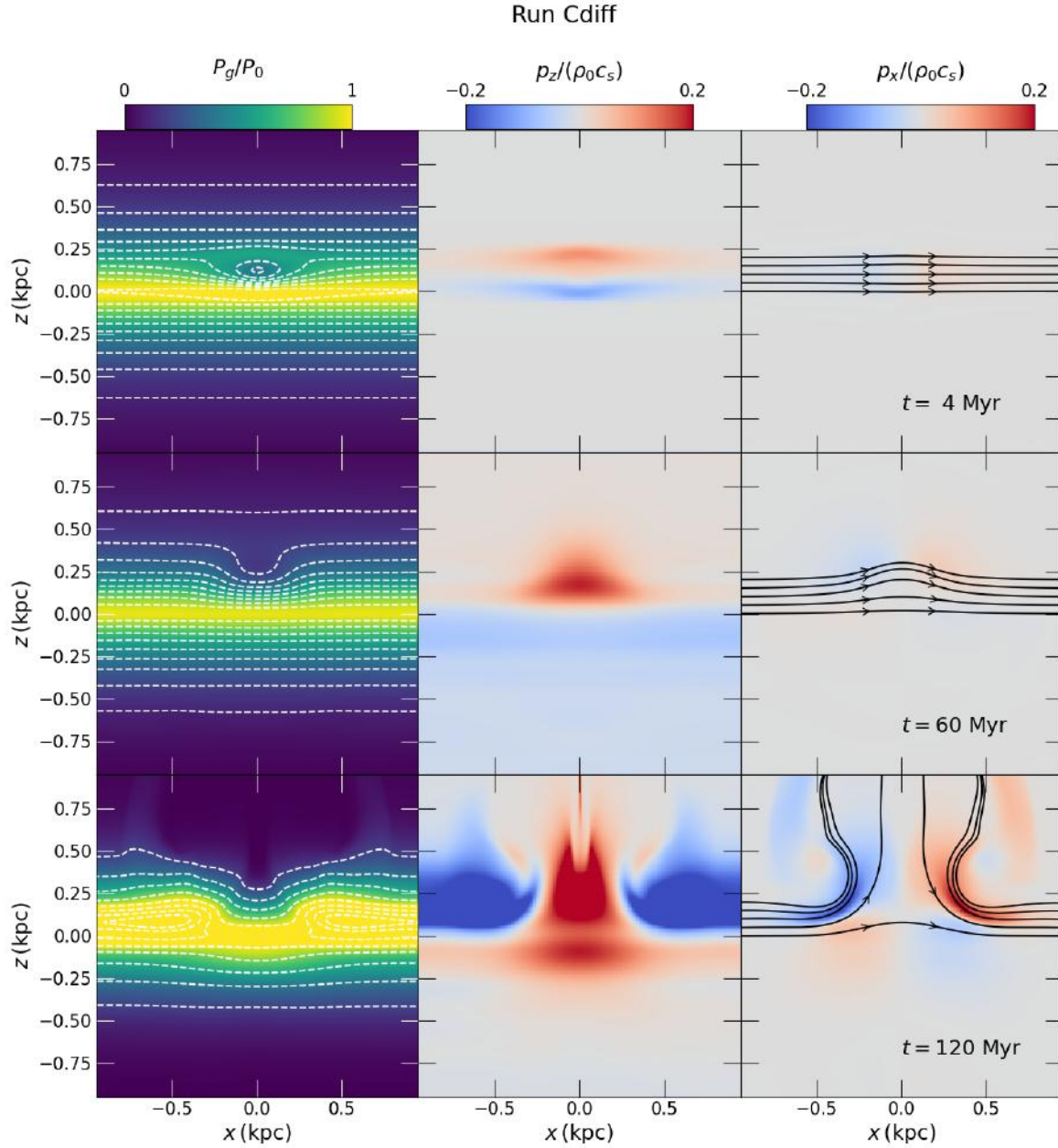
Figure 7. Plots of gas pressure (first column), vertical momentum (second column), and horizontal ($\hat{x}$) momentum (third column) at a $y = 0$ cut of simulation `C-adv`. In this simulation, the magnetic field is weaker and there is effectively no diffusion of cosmic rays. Early in the simulation, the cosmic rays are stuck to the thermal gas and build up a large over-pressured region (row 1). This over-pressure drives an explosion, which expands quickly upward, following the background density and pressure gradients. At later times (rows two and three), the explosion leaves an under-pressure region at $x = 0$ in the vertical half of the plane. This vacated region draws a flow up from the bottom half of the plane (bottom row). The normalization constants are $P_0 = 10^{-12} \, \mathrm{erg \, cm^{-3}}$ and $\rho_0 c_s = 10^{-18} \, \mathrm{g \, cm^{-2} \, s^{-1}}$. The white, dashed lines in the first column are density contours. The black lines in the third column are magnetic field lines.

Figure 8. Plots of gas pressure (first column), vertical momentum (second column), and horizontal momentum ($\hat{x}$) (third column) at a $y = 0$ cut of simulation B-str. The first row of plots, a time of 4 Myr after the injection, shows the injected cosmic rays streaming along the magnetic field lines, driving a front of gas. This front of gas results in a low density region near $x = 0$ along the field lines. This region buoyantly rises at subsequent times (second and third rows), driving more gas out from the $x = 0$ and causing the entire flux tube to rise. The normalization constants are $P_0 = 10^{-12}\,\mathrm{erg\,cm^{-3}}$ and $\rho_0 c_s = 10^{-18}\,\mathrm{g\,cm^{-2}\,s^{-1}}$. The white, dashed lines in the first column are density contours. The black lines in the third column are magnetic field lines.

Figure 9. Plots of gas pressure (first column), vertical momentum (second column), and horizontal ($\hat{x}$) momentum (third column) at a $y = 0$ cut of simulation C-diff. In this simulation, cosmic ray diffusion is the dominant transport mechanism. Early in the simulation, the cosmic rays quickly diffuse along the magnetic field lines. This diffusion leaves a significant underpressured, under dense region near $x = 0$. This region begins to rise buoyantly, shown in the middle row. The final row shows gas has fallen back toward the disk in the region around the injection, while the injection has created an under-dense column near $x = 0$. The normalization constants are $P_0 = 10^{-12}\,\mathrm{erg\,cm^{-3}}$ and $\rho_0 c_s = 10^{-18}\,\mathrm{g\,cm^{-2}\,s^{-1}}$. The white, dashed lines in the first column are density contours. The black lines in the third column are magnetic field lines.
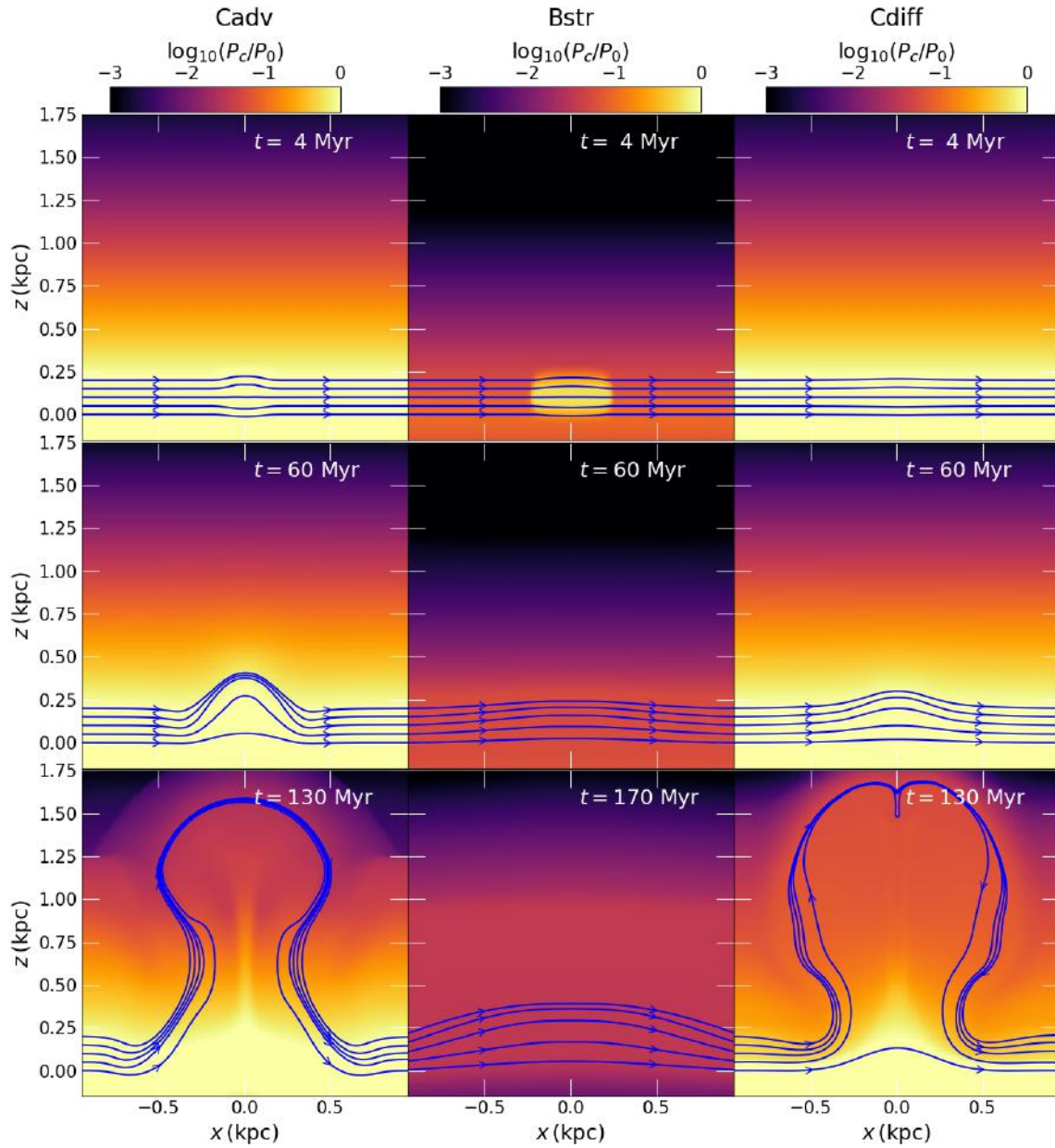
Figure 10. Plots of cosmic ray pressure at a $y = 0$ cut of simulations C-adv (first column), B-str (second column), and C-diff (third column). The normalization constant is $P_0 = 10^{-12} \, \text{erg} \, \text{cm}^{-3}$. The blue lines are magnetic field lines. In the first two rows, cuts are all from the same time snapshots, but the final row shows simulation B-str at a later time snapshot than the other two simulations. The vertical gradient becomes less steep in simulation B-str, and the gradient is significantly disrupted in both simulations C-adv and C-diff.

In this case, the flux tube immediately starts to rise buoyantly and gas is very quickly pushed off the flux tube. Cosmic ray pressure takes longer to follow the decrease of mass and magnetic pressure. After $\sim 110\,$Myr, the top of the flux tube has reached the upper bound of the simulation, and the tube-averaged values start to be less useful as a result of this interaction with the upper boundary. While this simulation highlights the effectiveness of thermal energy injection, our simulations lack radiative cooling. This injected, hot gas should cool by emitting radiation while it expands. We estimate a radiative cooling time scale determine the effect of radiative cooling on the injection, using Eqn. 34.4 from Draine (2011):

$$t_{\rm cool} = 1.1 \cdot 10^5\,{\rm yr} \left(\frac{T}{10^6\,{\rm K}} \right)^{1.7} \left(\frac{n_{\rm H}}{{\rm cm}^3} \right)^{-1} \qquad (26)$$

For simulation U-therm, the peak temperature in the center of the injection is $10^{5.04}\,$K, compared to the background $T_0 = 10^{3.86}\,$K Therefore, the radiative cooling time for this injection is $t_{\rm cool} \approx 2.2\,$kyr. This time scale is so short that this thermal injection should dissipate before causing a disruption in the ISM like we see in simulation U-therm. While temperatures are even higher in actual supernova remnants ($\sim 10^7\,$K for the Sedov-Taylor phase (Draine 2011)), our injection represents a long term average impact of those remnants. The fundamental point is that radiative cooling will limit the impact of the thermal injection, as compared to a cosmic ray injection. A similar effect is seen in models of supernova heated gas launched from galactic disks, which tend to be fountains rather than winds (Emerick et al. 2016).

5. DISCUSSION: SIMULATION COMPARISON

To the questions posed in Sec. 1, we have the following answers:

- (Q1) A purely Parker stable medium limits the effect of cosmic ray injection. An isothermal medium is more prone to disruption by cosmic ray. See Fig. 11.

- (Q2) Cosmic ray advection and diffusion drive changes in the ISM on short time scales, through explosive launching and buoyancy, respectively. Cosmic ray streaming delays the flux tube's rise, but eventually causes buoyant rising. See Fig. 12.

- (Q3) Stronger injections drive more explosive flows, and injections closer to the midplane take longer to launch the flux tube. See Fig. 13.
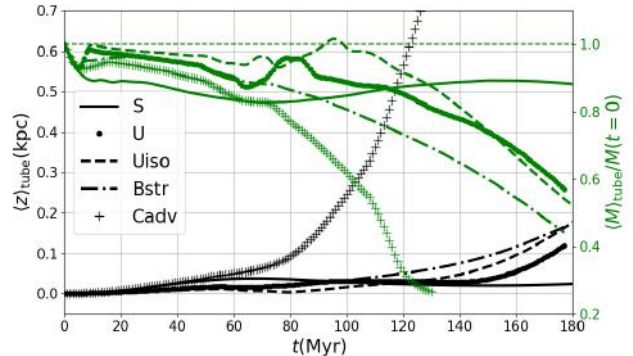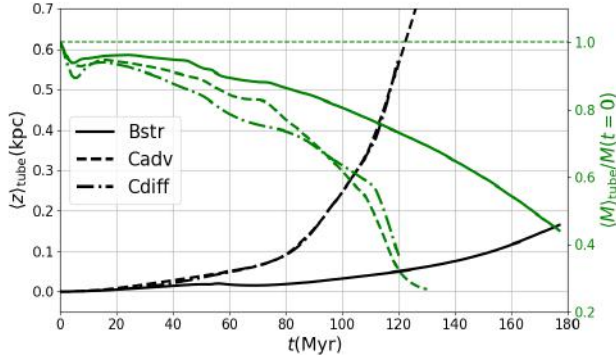

Figure 11. Plot of average tube height (black) and mass (green) for simulations related to Q1. Note the vertical axis has been extended compared to Figs. 4, 5, 6. Solid lines are show simulation S, circle markers show simulation U, dashed lines show simulation U-iso, dotted lines show simulation B-str and plus markers show simulation C-adv. The streaming dominated simulations, U and B-str, rise late. The advection dominated simulations, C-adv and S, have different results. The primary difference is in their total value of $\alpha + \beta$. Simulation U-iso with $\gamma_g = 1.1$ allows a more mass loss later in the simulation, when compared with simulation U which had $\gamma_g = 5/3$.

- (Q4) Thermal injection drives buoyant rising of the flux tube on a shorter time scale than cosmic ray injection. Cosmic rays decrease the average mass along the flux tube at a slower rate. Eventually, cosmic ray injections overtake thermal injections in height. See Figs. 13, 14, 15.

In the following subsections, we defend these answers and provide more complete explanations.

5.1. *Dependence on Background Medium (Q1)*

We explored how changes in the background medium affected the evolution of a cosmic ray injection. The results are shown in Fig. 11, which plots the average mass and height along the flux tube of each simulation.

The Parker stable simulation (Simulation S) weathers the cosmic ray injection, at least under transport by advection and streaming, reaching a new stable equilibrium. When the background is Parker unstable according to the original criterion (Eqn. 9), the injection drives significant change. For the simulations U, B-str, and C-adv, we can use Eqn. 9 to show the combined nonthermal pressures dominate the gas compressibility $(\alpha + \beta = 2) > (\gamma_g - 1 = 2/3)$. The simulations with a background biased towards magnetic pressure (B-str) or cosmic ray pressure (C-adv) launch the flux tube faster than the equipartition case (U). Therefore, the initial nonthermal pressures, given by (α, β), determine how prone the system is to disruption by cosmic ray

Figure 12. Plot of average tube height (black) and mass (green) for simulations related to Q2. Note the vertical axis has been extended compared to Figs. 4, 5, 6. Solid lines are show simulation `B-str`, circle markers show simulation `C-adv`, and plus markers show simulation `C-diff`. The streaming case has the flux tube rise buoyantly, but only after a long time $\gtrsim 100\,\mathrm{Myr}$. In contrast, the advection and diffusion dominated cases rise early $\lesssim 100\,\mathrm{Myr}$ and cause a significant amount of mass loss from the flux tube.

injection. This dependence also suggests an ISM with non-uniform α, β would provide a complex environment for cosmic ray injection, since different directions and positions could be more (or less) prone to being disrupted.

The case of an isothermal-like background with $\gamma_g = 1.1$ responds on a slightly shorter timescale than a background medium with $\gamma_g = 5/3$. This conclusion comes from considering the average height achieved by the flux tubes in simulations `U-iso` and `U`. In simulation `U-iso`, buoyant rising begins after 80 Myr and stays significant through the end of the simulation. For simulation `U`, buoyant rising becomes dominant only after 140 Myr. The average mass also decreases at a faster rate at late times in simulation `U-iso`. Because γ_g is lower, it takes less work to compress the gas and push it off the flux tube once buoyancy kicks in. This change allows mass to flow at a faster rate, driving the buoyancy force to become larger.

5.2. Dependence on Cosmic Ray Transport (Q2)

We ran three Parker unstable simulations, each with a different dominant cosmic ray transport mechanism: simulation `B-str` is streaming dominated, simulation `C-adv` is advection dominated, and `C-diff` is diffusion dominated. With these simulations, it is clear that streaming does a poor job of launching material when compared to diffusion and advection, which both disrupt the ISM on a short time scale $\sim 10\,\mathrm{Myr}$. Fig. 12 shows the flux tube averaged mass and height for these three simulations.

Simulation B does not start to rise buoyantly until a significant amount of mass has been lost from the flux tube. In comparison, the buoyant rise in simulation `C-diff` (see bottom panel of Fig. 5, where peak and average height track along each other) happens quickly. This buoyancy is the result of a large density hole carved by the cosmic ray injection (see Fig. 9). A smaller hole is created in the streaming simulation, delaying the rise of the flux tube (see Fig. 8). The advective simulation `C-adv` is mainly driven by an explosive launching, instead of buoyancy. However, it and the diffusion case produce similar results in terms of flux tube movement. The difference between these simulations is more apparent in the beginning of the simulations, when the launching is different. This difference is seen in the top rows of Figs. 7 & 9.

Of these simulations, the diffusion case is the most surprising. At the beginning, we suggested cosmic ray diffusion may have a smaller effect on feedback processes than streaming and advection, because there is less time for cosmic rays to impact the ISM. However, our simulation `C-diff` shows a large cosmic ray injection can generate enough force through the cosmic ray pressure gradient to move mass out of the disk and bend the magnetic field to be perpendicular to the galactic disk.

5.3. Dependence on Injection Characteristics (Q3 & Q4)

We ran three simulations focused on the injection characteristics. The first, `U-heavy`, placed the injection lower in the galactic disk. Other than rising later than other simulations, this simulation gave similar results when compared to `U`. Simulation `U-blast` examined how increasing the injection energy to 10^{52} erg would change the dynamics. This large injection caused significant change in the ISM, causing the flux tube to rise rapidly. In Simulation `U-therm`, we replaced the cosmic ray injection with a thermal injection of similar magnitude. This injection contained no mass, but was an over-pressure ($T \sim 10^5\,\mathrm{K} > T_0 \sim 10^4\,\mathrm{K}$) region. This thermal energy injection caused rapid mass flow off the flux tube, driving a buoyant rise. The tube averaged mass and height of these simulations are shown as part of Fig. 13.

5.4. Fast Disruption: Cosmic rays vs. Thermal Injection

The simulations which produced the largest changes in the shortest time for an injection energy 10^{51} erg were `C-adv`, `C-diff`, and `U-therm`. These injections had flux tubes rise in short times $\lesssim 100\,\mathrm{Myr}$, and caused the flux tube to lose approximately half its mass on that same timescale. In Fig. 14 we show the evolution of peak and
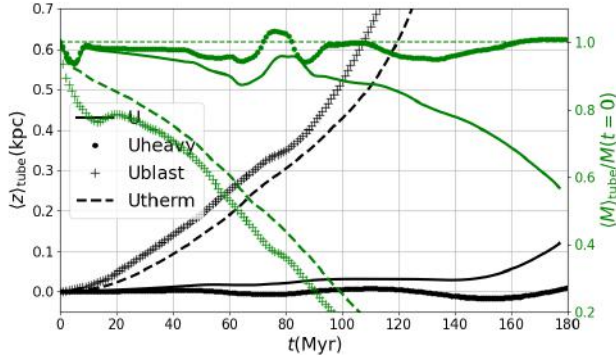
Figure 13. Plot of average tube height (black) and mass (green) for simulations related to Q3 and Q4. Note the vertical axis has been extended compared to Figs. 4, 5, 6. Solid lines show simulation U, circle markers show simulation U-iso, plus markers show simulation U-heavy, and dashed lines show simulation U-blast. Simulation U-heavy does eventually rise from the disk after 200 Myr. Simulation U-blast drives an explosive launching faster than the thermal injection in U-therm.
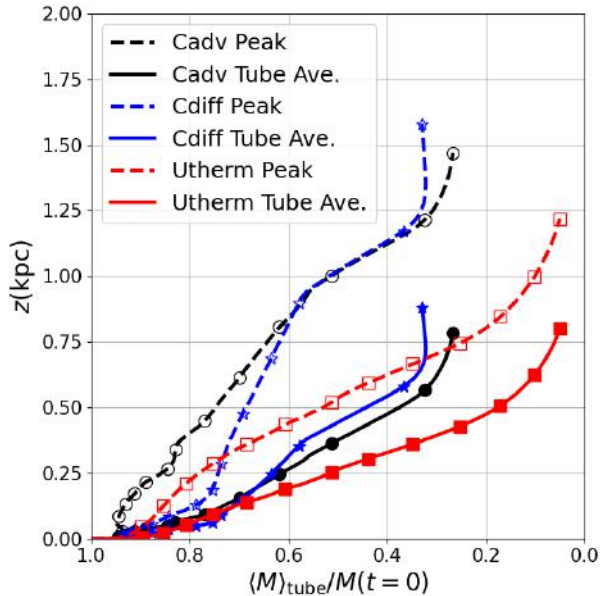

Figure 14. The evolution over time of each flux tube's height and mass. Dashed lines and open markers correspond to the flux tube's peak height, whereas solid lines and filled markers correspond to the tube's average height. Each simulation is shown until 130 Myr, with markers placed at 10 Myr increments. Black circles show simulation C-adv, blue stars show simulation C-diff, and red squares show simulation U-therm. While the thermal injection in simulation U-therm initially moves material up faster, at late times the cosmic ray injections in simulations C-adv and C-diff overtake simulation U-therm. After 130 Myr, the diffusion transported cosmic ray injection has created the most extended outflow.

average tube height against mass. The markers on each line denote 10 Myr steps, whereas the points making up each line are made with a resolution of 1 Myr. The final point is at 130 Myr for each simulation. Even though the cosmic ray injection simulations take a longer time to start rising, they rise at a faster rate than the thermal injection. They overtake the thermal injection after approximately 90 Myr, and they have more mass at that time. This final point, 130 Myr is shown in Fig. 15 for the three simulations. Fig. 15 shows density of each fast simulation at $y = 0$, and illustrates that each produces a different magnetic field structure. So, not only do the simulations evolve in different ways (see Fig. 14), but also they produce different long term effects. Considering simulation U-therm is an overestimate of thermal injection's impact (see cooling time argument in Sec. 4.9), we can focus on the difference between C-adv and C-diff. The left and middle plots in Fig. 15 show that cosmic ray transport changes the both the flow of gas around the rising flux tube and the shape of the magnetic field lines. Additionally, the thin inner region of rising material in simulation C-diff has a steeper density gradient, and we do not resolve it enough to reliably analyze the dynamics of this plume of gas. The exact dynamics of this region created by the rising flux tube could be important for understanding outflows from galactic disks.

6. CONCLUSION

We ran nine simulations of cosmic ray injection into a vertically stratified medium, using the Athena++ code. These simulations illustrated the effect of cosmic ray injection in a galactic disk, on intermediate scales ($\sim$ 1 kpc) larger than the ISM's fine structure and smaller than the entire galaxy. By exploring an extended parameter space, we produced the most detailed picture yet of localized cosmic ray injection. We also showed that cosmic ray transport dictates the impact of cosmic rays on the ISM. Below, we provide the key points and results of this work:

1. Cosmic ray diffusion of a cosmic ray injection can change the ISM's vertical structure and a galaxy's magnetic field on timescales < 100 Myr.

2. Heating from cosmic ray streaming by a cosmic ray injection had little large scale effect on time scales $\lesssim 200$ Myr.

3. A flux tube disrupted by cosmic ray injection will rise faster at later times than one disrupted by thermal injection, producing a larger mass flow of material out of the galactic disk.

Our simulations provided useful heuristic results by considering cosmic ray injection in a stratified medium.
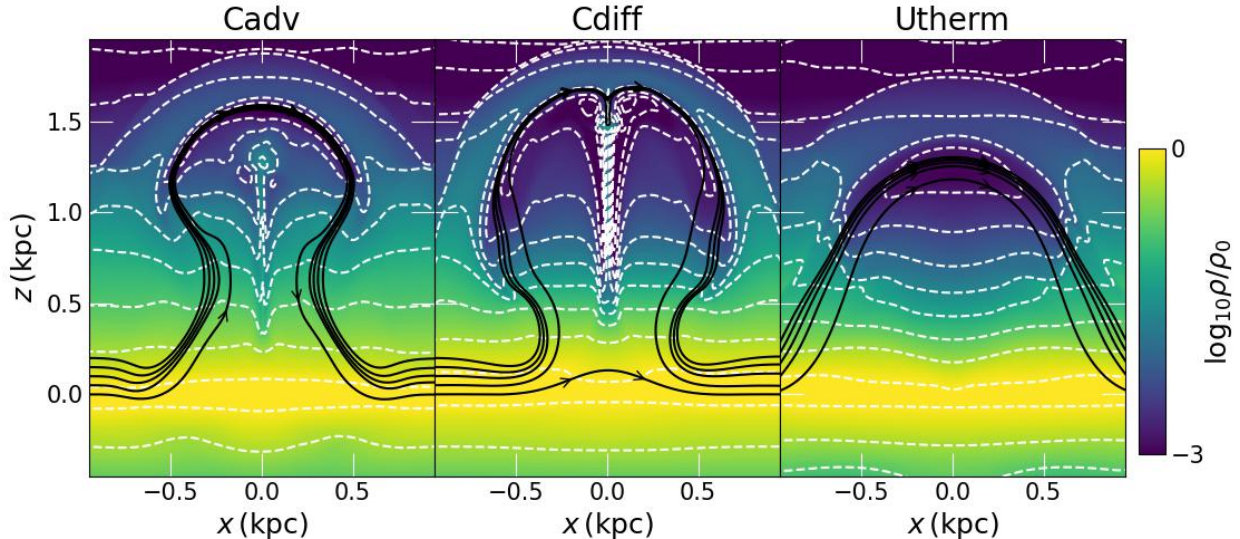
Figure 15. Cuts of simulations `C-adv`, `C-diff`, and `U-therm`. These simulations were the most efficient at launching material out of the disk, and these plots of density at a time of $130\,\mathrm{Myr}$ illustrate an energy injection can disrupt the vertical structure of a galactic disk. The black lines are magnetic field lines and the white dashed lines are density contours. These plots are cuts of our 3D simulations at $y = 0$. The most intense mass movement appears in `C-diff`, where the contours show a very low density flux tube stretched into a shell which lifts some cold, dense gas out of the disk.

These simulations are clearly limited in their realism because galactic disks are not uniformly stratified. The ISM in galactic disks is multiphase and clumpy. Additionally, by neglecting the dynamics of the stellar gravitational potential, we lack forcing terms which could change the effects of these energy injections. Future work should focus on diffusion as the primary cosmic ray transport mechanism, along with implementation of more realistic ISM conditions (varying gravitational field strength, multiple gas phases, galactic rotation, etc.). The non-constant α, β of the injection have a significant impact. This non-uniformity should be extended to the background medium, instead of using the constant α, β assumption originally introduced by Parker (1966).

In these simulations, we neglected radiative heating and cooling, but those processes are an important consideration in the ISM. The radiative cooling would be particularly important for the gas heated by cosmic ray streaming. Cooling will minimize, and possibly remove, the impact of the thermal injection in simulation `U-therm`. Additionally, multiple supernovae going off in the exact same volume at the exact same time is unlikely. In future work, we will aim to resolve the injection into multiple injections at different times and locations. Separating the injections in space opens up a variety of other situations which make it difficult to isolate the buoyancy the injection creates, hence why we only considered a single injection location in this work. For example, explosions nearby one another in the xy plane but on opposite sides of the midplane could sig-

nificantly compress gas at $z = 0$, which may then drive its own flow if the density and pressure gradients are large enough.

For large scale (cosmological or galactic) simulations, there needs to be some consideration of cosmic ray injection. Even simulations which include cosmic rays generally do not include the impact of their injection into the ISM. Our work shows they can drive an upward flow in $< 100\,\mathrm{Myr}$ after their injection, and most of that upward movement actually happens in $< 20\,\mathrm{Myr}$. Since the upward flow expands out along the magnetic field line direction, a subgrid model would not be necessary. A resolution of $\sim 100\,\mathrm{pc}$ would be enough to produce an upward flow like what we see here (consider Fig. 15). In the y direction, across the magnetic field and in the plane of the disk, higher resolution would be necessary. The width of the flux tube barely reaches $100\,\mathrm{pc}$ in that direction, and the overall dynamics in that direction are minimal. The main impact the y direction had in our simulations is to allow mass above the flux tube to move out of the path of the rising flux tube. The actual resolution of that dimension is less significant.

Our work also shows cosmic ray injection is an important part of dynamics in a galaxy. Moving, heating, and compressing gas all have an impact on where stars form and on galactic structure. Since the eventual rise of the flux tube happens in a short time ($< 20\,\mathrm{Myr}$), the dynamics created by cosmic ray injection would not be washed out by galactic rotation and other dynamical processes. In fact, the delay of the quick rise from the

initial injection provides an interesting setup for galactic dynamics. If the parcel of gas we consider passes through a spiral density wave, and there the cosmic ray injection happens due multiple supernova explosions, then the parcel will have left the spiral density wave before the injection causes dynamical effects. Therefore, the heating, compression, and movement of gas would be happening in lower luminosity regions of disk galaxies with well defined spiral arms. In future work, we plan to introduce spiral density waves by adjusting our gravitational acceleration profile, to see if the process above occurs and has observational consequences. Our results also shed light on the respective roles of cosmic ray compressibility and buoyancy alluded to in Sec. 2.1. The constant (α, β) model appears to be somewhat special

in that differential loading of cosmic rays onto magnetic flux tubes and time dependent flows create conditions under which buoyancy dominates. Including these time and space localized effects in global simulations is an important challenge for the future.

REFERENCES

Asseo, E., Cesarsky, C. J., Lachieze-Rey, M., & Pellat, R. 1978, ApJL, 225, L21, doi: 10.1086/182784

Boulares, A., & Cox, D. P. 1990, ApJ, 365, 544, doi: 10.1086/169509

Breitschwerdt, D., McKenzie, J. F., & Voelk, H. J. 1991, A&A, 245, 79

Bustard, C., & Zweibel, E. G. 2021, ApJ, 913, 106, doi: 10.3847/1538-4357/abf64c

Caprioli, D., & Spitkovsky, A. 2014, ApJ, 783, 91, doi: 10.1088/0004-637X/783/2/91

Chan, T. K., Kereš, D., Hopkins, P. F., et al. 2019, MNRAS, 488, 3716, doi: 10.1093/mnras/stz1895

Draine, B. T. 2011, Physics of the Interstellar and Intergalactic Medium (Princeton University Press)

Emerick, A., Mac Low, M.-M., Grcevich, J., & Gatto, A. 2016, ApJ, 826, 148, doi: 10.3847/0004-637X/826/2/148

Everett, J. E., Zweibel, E. G., Benjamin, R. A., et al. 2008, ApJ, 674, 258, doi: 10.1086/524766

Farber, R., Ruszkowski, M., Yang, H. Y. K., & Zweibel, E. G. 2018, ApJ, 856, 112, doi: 10.3847/1538-4357/aab26d

Ferrière, K. M. 2001, Reviews of Modern Physics, 73, 1031, doi: 10.1103/RevModPhys.73.1031

Fryxell, B., Olson, K., Ricker, P., et al. 2000, ApJS, 131, 273, doi: 10.1086/317361

Giz, A. T., & Shu, F. H. 1993, ApJ, 404, 185, doi: 10.1086/172267

Hanasz, M., & Lesch, H. 2000, ApJ, 543, 235, doi: 10.1086/317077

—. 2003, A&A, 412, 331, doi: 10.1051/0004-6361:20031433

Hanasz, M., Lesch, H., Naab, T., et al. 2013, ApJL, 777, L38, doi: 10.1088/2041-8205/777/2/L38

Heintz, E., Bustard, C., & Zweibel, E. G. 2020, ApJ, 891, 157, doi: 10.3847/1538-4357/ab7453

Heintz, E., & Zweibel, E. G. 2018, ApJ, 860, 97, doi: 10.3847/1538-4357/aac208

Hopkins, P. F., Wetzel, A., Kereš, D., et al. 2018, MNRAS, 480, 800, doi: 10.1093/mnras/sty1690

Jiang, Y.-F., & Oh, S. P. 2018, ApJ, 854, 5, doi: 10.3847/1538-4357/aaa6ce

Jiang, Y.-F., Stone, J. M., & Davis, S. W. 2014, ApJS, 213, 7, doi: 10.1088/0067-0049/213/1/7

Kempski, P., & Quataert, E. 2021, arXiv e-prints, arXiv:2109.10977. https://arxiv.org/abs/2109.10977

Kulsrud, R., & Pearce, W. P. 1969, ApJ, 156, 445, doi: 10.1086/149981

Mouschovias, T. C. 1974, ApJ, 192, 37, doi: 10.1086/153032

Newcomb, W. A. 1961, Physics of Fluids, 4, 391, doi: 10.1063/1.1706342

Parker, E. N. 1966, ApJ, 145, 811, doi: 10.1086/148828

Rodrigues, L. F. S., Sarson, G. R., Shukurov, A., Bushby, P. J., & Fletcher, A. 2016, ApJ, 816, 2, doi: 10.3847/0004-637X/816/1/2

Ruszkowski, M., Yang, H. Y. K., & Zweibel, E. 2017, ApJ, 834, 208, doi: 10.3847/1538-4357/834/2/208

Ruzmaikin, A., Sokolov, D., & Shukurov, A. 1988, Nature, 336, 341, doi: 10.1038/336341a0

Sharma, P., Colella, P., & Martin, D. F. 2010, SIAM Journal on Scientific Computing, 32, 3564, doi: 10.1137/100792135

Skilling, J. 1975, MNRAS, 172, 557, doi: 10.1093/mnras/172.3.557

Stone, J. M., Tomida, K., White, C. J., & Felker, K. G. 2020, The Astrophysical Journal Supplement Series, 249, 4, doi: 10.3847/1538-4365/ab929b

Uhlig, M., Pfrommer, C., Sharma, M., et al. 2012, MNRAS, 423, 2374, doi: 10.1111/j.1365-2966.2012.21045.x

Wentzel, D. G. 1969, ApJ, 156, 303, doi: 10.1086/149965

Wiener, J., Oh, S. P., & Zweibel, E. G. 2017, MNRAS, 467, 646, doi: 10.1093/mnras/stx109

Zhang, D. 2018, Galaxies, 6, 114, doi: 10.3390/galaxies6040114

Zweibel, E. G. 2017, Physics of Plasmas, 24, 055402, doi: 10.1063/1.4984017

Zweibel, E. G., & Kulsrud, R. M. 1975, ApJ, 201, 63, doi: 10.1086/153858

APPENDIX

A. BOUNDARY CONDITIONS

With the goal of minimizing numerical errors, simulations often exploit periodic boundary conditions. In the current example, using periodic boundaries at every interface is difficult because we are studying a stratified medium. We also do not want to deal with a shock at the boundaries when the injected material reaches the boundary. Therefore, we need non-periodic boundary conditions in the direction of gravity ($\hat{z}$) and in the primary propagation direction of the injected material: along the magnetic field ($\hat{x}$). In an effort to keep symmetry in the midplane of the simulation, the boundary conditions in the $\hat{y}$ direction are the same as those of the $\hat{x}$ direction. This coordinate system is depicted in Fig. 1

In the direction of stratification ($\hat{z}$), we use vacuum (also known as diode) boundary conditions. These conditions make it impossible for inflow to occur, since the boundary cells are set to the density and pressure floor of the numerical simulation. We also avoid setting up a steep discontinuity at this boundary by extending the simulation several scale heights in the vertical direction. Because of this extension, the cells near the boundary are already almost at the density and pressure floors when the simulation starts. Then, any dynamical activity beyond that initial equilibrium profile will propagate out of the simulation.

In the direction of the magnetic field ($\hat{x}$) we use outflow boundary conditions. While these allow inflow from boundary cells after the crest of a wave passes the boundary, there is very little error if the gas is quickly moving out of the simulation at that boundary. Our current problem satisfies this assumption because the flow is either static, or large (when the perturbation pushes gas down a magnetic flux tube and toward the boundary). Ideally, we would again use vacuum boundary conditions to stop inflow. However, we cannot us a vacuum in this direction since this would create a significant discontinuity near the midplane of the simulation, where there are gas densities and pressures above the floor values. This boundary discontinuity would drive a non-physical outflow from the simulation and create a systematic error in our estimate of flux tube buoyancy. The outflow condition, while worse at handling outflow than the vacuum conditions, can handle outflow from non-vacuum media. This justification shows the outflow boundary is the best boundary condition available for the magnetic field direction ($\hat{x}$).

B. SIMULATION CONVERGENCE

There are non-physical parameters we must choose to run the simulations. However, changing them affects the simulation results. To mitigate the significance of these parameters we performed several convergence tests.
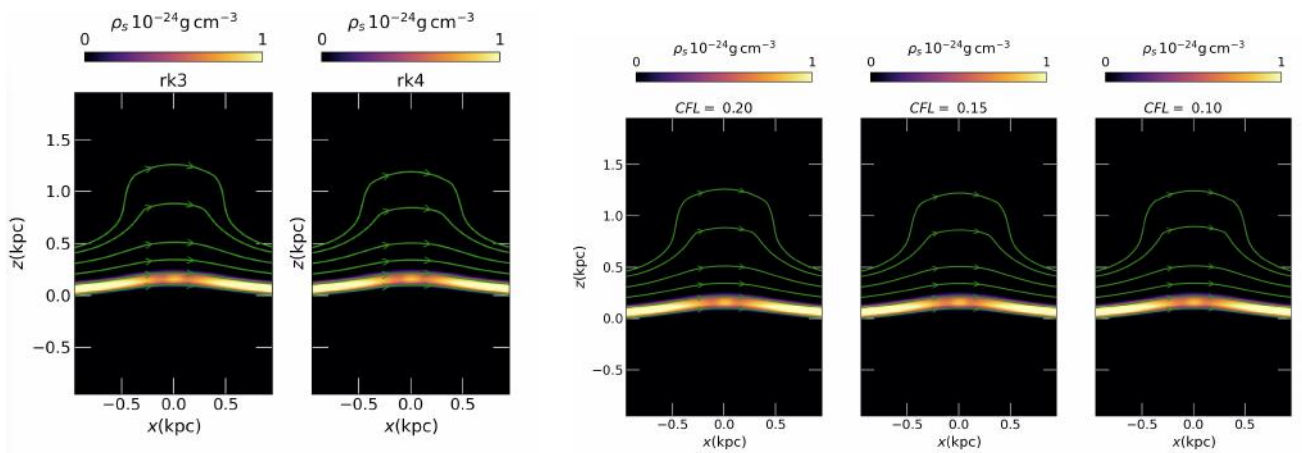

Figure 16. Convergence of time integrator (left two plots) and CFL number (right three plots). These convergence simulations were 2D, used a weak injection strength of 10^{50} erg, and are pictured 200 Myr after the cosmic ray injection. The scalar dye is shown in units of 10^{-24} g cm^{-3}. The scalar dye was initialized on a flux tube containing the cosmic ray injection. Magnetic field lines are shown in green. The vertical $\hat{z}$ and horizontal $\hat{x}$ axes are shown in units of 1 kpc. These simulations justified our choice of a 3rd order Runge Kutta time integrator (rk3) and a CFL number of 0.2 in the 3D simulations presented in this work.
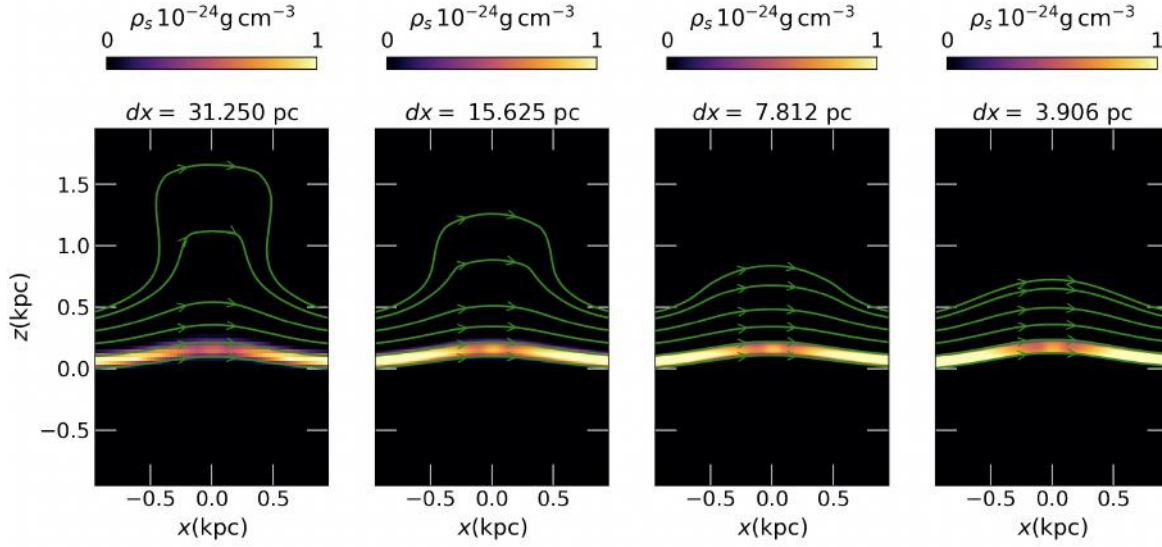
Figure 17. Convergence of resolution. These convergence simulations were 2D, used a weak injection strength of 10^{50} erg, and are pictured 200 Myr after the cosmic ray injection. The scalar dye is shown in units of 10^{-24} g cm^{-3}. The scalar dye was initialized on a flux tube containing the cosmic ray injection. Magnetic field lines are shown in green. The vertical $\hat{z}$ and horizontal $\hat{x}$ axes are shown in units of 1 kpc. These simulations justified our choice of a resolution of 10 pc in the 3D simulations, because the scalar dye is consistent with the results from higher resolutions.

The first test considered whether we needed to perform 3D simulations, as well as what the necessary length was in that third direction ($\hat{y}$ in Fig. 1). Our test looked at the height of the flux tube over time, after the injection. We found the flux tube took longer to rise in 2D simulations, and realized this difference was because the third dimension allowed mass above the rising flux tube to move out of the way. In the 2D simulations, the rising flux tube had to lift all the gas above itself. This increased weight slowed the rise of the flux tube, and led us to use 3D simulations for the main exploration.
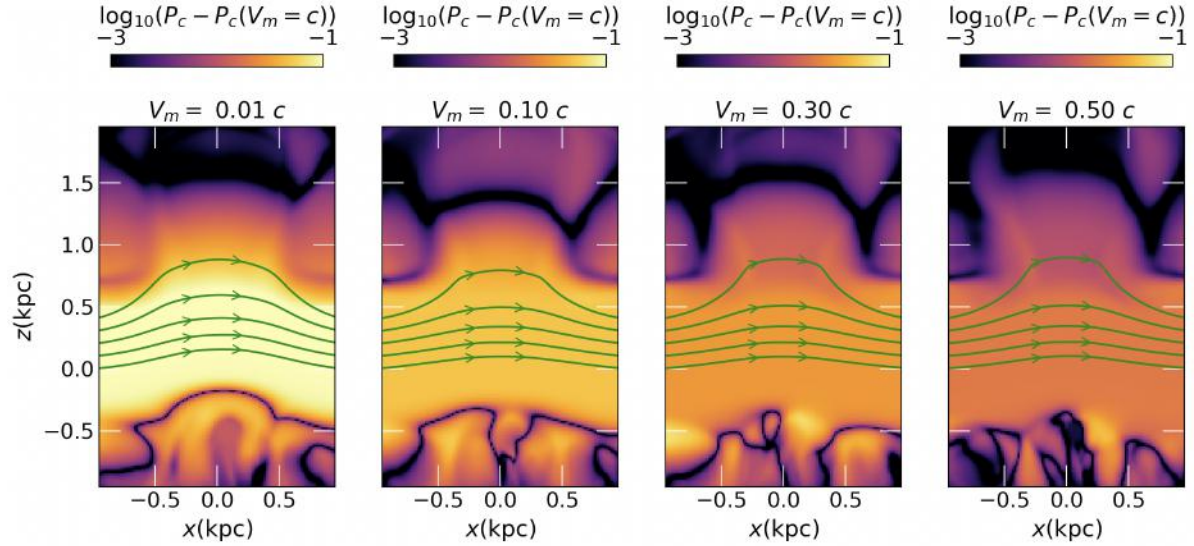

Figure 18. Convergence of the reduced speed of light parameter. These convergence simulations were 2D, used a weak injection strength of 10^{50} erg, and are pictured 200 Myr after the cosmic ray injection. The absolute value of error in cosmic ray pressure is shown for each simulation, 200 Myr after cosmic ray injection. The simulation with $V_m = c$ is not shown since the plot would be blank. With $V_m = 0.3c$, the error in the region of interest (where magnetic fields are plotted in green) has dipped below 1%. For the 3D simulations presented in this paper, we used $V_m = 0.3c$.

The second test used 2D simulations to narrow our choice of several numerical parameters: time integrator, Courant-Friedrich-Lewy (CFL) number, resolution, and the reduced speed of light constant V_m in Eqn. 24. Using 2D simulations allowed us to save computational resources while exploring the convergence of these simulations. The first test proved the 2D simulations would be less accurate because they limit the movement of magnetic flux tubes, but most of the fast, dynamic flow is still in the xz-plane. For numerical parameters, the motion in that plane is where we need be concerned. All the convergence tests here used a weak injection of 10^{50} erg with other parameters equal to those of simulation U. With the weaker injection and 2D restricted motion, the flux tube has just begun to rise buoyantly by 200 Myr.

The time integrator choice of 3rd order Runge-Kutta and CFL number (0.2) were well converged, as there was little to no change in the results 200 Myr after the cosmic ray injection. The convergence of these parameters is shown in Fig. 16.

The resolution and reduced speed of light constant required more extensive convergence studies. Changing resolution significantly changed the time scale and resulting dynamics. We varied resolution over a multiplicative factor of 8, and the results for the evolution of the density of scalar dye are shown in Fig. 17. We decided to use a resolution of 10 pc, optimizing accuracy and computational time. For the middle resolutions in Fig. 17 the scalar dye and height of the flux tube are very similar after 100 Myr. We do not expect the magnetic field lines, integrated after the simulation, to match exactly when comparing across resolutions.

Changing the reduced speed of light significantly changed the simulation dynamics. For each value of V_m, we compare to a simulation where we used $V_m = c$. In Fig. 18, we plot a colormap of error in cosmic ray pressure P_c with respect to the speed of light case $P_c(V_m = c)$. We chose a value of $0.3c$ since the error barely peaked above 1% in parts of that simulation, after 200 Myr. The asymmetric, thin transitions in error in the lower half of the simulations are a result of our plotting the absolute value of the error. The error getting small is more importantly where the error switches sign. The average error where the field lines are plotted are a more useful measure of accuracy in this parameter study, because resolution is constant. We chose $0.3c$ based of that region of these error maps.